inorganics

MDPI

Review

Aluminum-Nitride-Based Semiconductors: Growth Processes, Ferroelectric Properties, and Performance Enhancements

Luyi Wang [1], Jinhong Cheng [1], Ke Qu [1,2,*], Qingfeng Zhu [2], Bobo Tian [1,*] and Zhenzhong Yang [1,*]

[1] Key Laboratory of Polar Materials and Devices (MOE), Shanghai Center of Brain-Inspired Intelligent Materials and Devices, Department of Electronics, East China Normal University, Shanghai 200241, China; 51214700090@stu.ecnu.edu.cn (L.W.); chjh37242@163.com (J.C.)

[2] Guangdong Provincial Key Laboratory of Electronic Functional Materials and Devices, Huizhou University, Huizhou 516001, China

* Correspondence: kqu@chem.ecnu.edu.cn (K.Q.); bbtian@ee.ecnu.edu.cn (B.T.); zzyang@phy.ecnu.edu.cn (Z.Y.)

Abstract: Aluminum nitride (AlN)-based ferroelectric films offer significant advantages, including compatibility with CMOS back-end processes, potential for sustainable miniaturization, and intrinsic stability in the ferroelectric phase. As promising emerging materials, they have attracted considerable attention for their broad application potential in non-volatile ferroelectric memories. However, several key scientific and technological challenges remain, including the preparation of single-crystal materials, epitaxial growth, and doping, which hinder their progress in critical ferroelectric devices. To accelerate their development, further research is needed to elucidate the underlying physical mechanisms, such as growth dynamics and ferroelectric properties. This paper provides a comprehensive review of the preparation methods of AlN-based ferroelectric films, covering AlN, $Al_{1-x}Sc_xN$, $Al_{1-x}B_xN$, $Y_xAl_{1-x}N$, and $Sc_xAl_yGa_{1-x-y}N$. We systematically analyze the similarities, differences, advantages, and limitations of various growth techniques. Furthermore, the ferroelectric properties of AlN and its doped variants are summarized and compared. Strategies for enhancing the ferroelectric performance of AlN-based films are discussed, with a focus on coercive field regulation under stress, suppression of leakage current, fatigue mechanism, and long-term stability. Then, a brief overview of the wide range of applications of AlN-based thin films in electronic and photonic devices is presented. Finally, the challenges associated with the commercialization of AlN-based ferroelectrics are presented, and critical issues for future research are outlined. By synthesizing insights on growth methods, ferroelectric properties, enhancement strategies, and applications, this review aims to facilitate the advancement and practical application of AlN-based ferroelectric materials and devices.

Keywords: aluminum-nitride-based semiconductors; growth; ferroelectric properties

check for updates

Academic Editor: Antonino Gulino

Received: 23 December 2024
Revised: 17 January 2025
Accepted: 18 January 2025
Published: 21 January 2025

Citation: Wang, L.; Cheng, J.; Qu, K.; Zhu, Q.; Tian, B.; Yang, Z. Aluminum-Nitride-Based Semiconductors: Growth Processes, Ferroelectric Properties, and Performance Enhancements. *Inorganics* **2025**, *13*, 29. https://doi.org/10.3390/inorganics13020029

Copyright: © 2025 by the authors. Licensee MDPI, Basel, Switzerland. This article is an open access article distributed under the terms and conditions of the Creative Commons Attribution (CC BY) license (https://creativecommons.org/licenses/by/4.0/).

1. Introduction

Aluminum nitride (AlN) is a new type of electronic ceramic material with excellent comprehensive performance. It has ultra-high thermal conductivity, excellent piezoelectricity, reliable electrical insulation performance, chemical stability, low dielectric loss, and a thermal expansion coefficient that matches that of semiconductor materials such as silicon [1–3]. It can break through the development bottleneck of the first- and second-generation semiconductor materials and is considered to be a third-generation semiconductor material. It has broad application prospects and a wide potential market in the fields of

electronics, electricity, locomotives, aviation and aerospace, national defense and military industry, communications, and many industrial fields [1,2].

AlN has a hexagonal wurtzite structure symmetrical along the c axis (Figure 1), with a $P6_3mc$ space group and two polarities, nitrogen (N) polarity and metal (M) polarity. The lattice constants are a = 3.112 Å and c = 4.982 Å. The structure is composed of tetrahedrons composed of Al atoms and N atoms, of which the three Al-N bonds along the a axis are B_1 bonds and the bonds along the c axis are B_2 bonds with lower energy, which are more likely to break [3]. This non-centrosymmetric crystal structure causes AlN to have spontaneous polarization, but it is broken down before the external electric field reaches the polarization reversal voltage. Although partial polarization reversal can be achieved by applying planar tensile stress and applying an electric field at high temperatures, it is currently difficult to achieve complete polarization reversal in undoped AlN at room temperature [4,5].

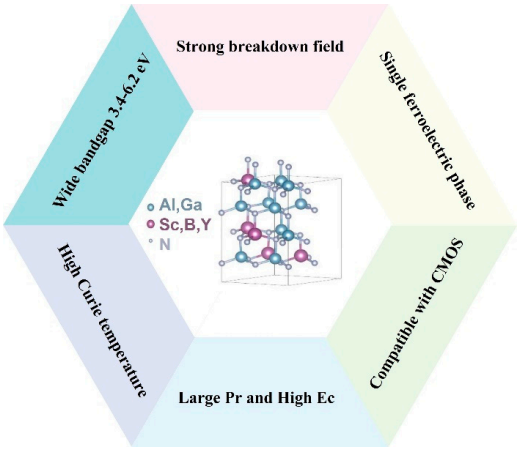

Figure 1. Crystal structure and ferroelectric properties of aluminum-nitride-based ferroelectric semiconductors.

Doping AlN with specific elements can effectively reduce the polarization reversal energy barrier at room temperature, transforming traditional III-nitride materials into ferroelectric candidates. Tasna'di et al. [6] believed that Sc-doped AlN flattens the overall energy landscape of the wurtzite structure, reducing the electric field required for switching from $P6_3mc$ to $P6_3/mmc$, that is, reducing the coercive field. Fichtner et al. [7] demonstrated ferroelectric polarization switching in sputtered AlScN with a remanent polarization (Pr) of 110 $\mu C/cm^2$ in 2019. Under the guidance of theory and experiment, more and more scholars have carried out a lot of research work and successfully synthesized a series of AlN-based ferroelectric films using techniques such as magnetron sputtering (MS), molecular beam epitaxy (MBE), metal–organic chemical vapor deposition (MOCVD), pulsed laser deposition (PLD), and atomic layer deposition (ALD). These include AlN [8–10], $Al_{1-x}Sc_xN$ [7,11], $Al_{1-x}B_xN$ [8,12], $Y_xAl_{1-x}N$ [13], and $Sc_xAl_yGa_{1-x-y}N$ [14]. Sputtered AlN-based films typically exhibit a high degree of c-axis-oriented texture but face challenges in achieving high crystal quality, including issues such as phase separation and abnormally oriented grains (AOG) [15]. In contrast, epitaxial techniques like MBE allow for finer control over purity, chemical composition, crystallinity, interface, and intercalation compared to traditional sputtering. However, dislocations in $Al_{1-x}Sc_xN$ films grown by MBE can lead to an overestimation of the remanent polarization, providing pathways for leakage current and lowering the breakdown voltage [16]. This underscores the critical importance of developing high-quality AlN-based films. This overview of the growth techniques for AlN and its doped derivatives aims to analyze how to select and optimize growth techniques and material design to overcome these challenges. Understanding

these processes will provide insights into exploring emerging doping strategies such as co-doping and nanostructure design.

The AlN ferroelectric films grown using the methods described above exhibit ultra-high Curie temperatures [17], substantial Pr (>100 μC/cm^2), and a wide, adjustable range of coercive field (Ec) (3.5–7.5 MV/cm). The Pr and Ec values are several times larger than those of hafnium-based ferroelectrics, have strong nonvolatility, and the band gap (4–6 eV) is much larger than that of $BiFeO_3$ (2–2.5 eV) [18]. Moreover, these films are compatible with mainstream semiconductor manufacturing processes, including Si and GaN, as well as complementary metal oxide semiconductor (CMOS) back-end technologies [19]. Doped AlN-based ferroelectric materials offer a promising path for the development of practical ferroelectric random access memory (FeRAM). Liu et al. [20] demonstrated a ferroelectric field-effect transistor (FE-FET) device, which integrates a ferroelectric AlScN dielectric layer with a two-dimensional MoS_2 channel. This device exhibited a stable storage state for up to 10^4 cycles and state retention for up to 10^5 s. Additionally, they used a fully CMOS-compatible, back-end-of-line (BEOL) process to fabricate a ferroelectric diode (FeD) based on $Al_{0.64}Sc_{0.36}N$ on a 4-inch Si wafer, achieving a large self-rectification ratio of >10^5 and a high on/off ratio of more than 50,000 [21]. Given their ferroelectric, pyroelectric, and piezoelectric properties, AlN-based semiconductors are poised to become key materials for a wide array of future applications, including high-frequency electronics [22], non-volatile memory (NVM) [23], and in-memory computing (IMC) [24]. However, the large coercive field and leakage current of these materials lead to elevated operating voltages and increased power consumption, presenting significant challenges for the durability and reliability of device-level applications [25]. Therefore, we focus on outlining the mechanisms and methods on how to improve the coercive field, leakage current, fatigue, and stability, hoping to obtain durable and reliable devices and realize commercialization as soon as possible.

This paper provides a comprehensive review of the development and properties of AlN-based ferroelectric semiconductor materials. It begins by discussing the characteristics of various AlN-based thin-film growth techniques, including MS, MBE, MOCVD, PLD, and ALD. Adjusting growth parameters such as temperature, gas pressure, gas flow, and power is essential to optimize the microstructure, morphology, and stress of the films to meet specific device design requirements. The paper then reviews the research progress of different AlN-based ferroelectric materials, highlighting experimental evidence supporting their ferroelectric properties. This includes findings from electrical testing, observations of ferroelectric domains, unit cell polarity analysis, and atomic-level polarization switching. The ferroelectric characteristics of various materials are summarized and compared. This paper further delves into the mechanisms behind key challenges, such as stress-regulated coercive fields, leakage currents, and fatigue, which present significant barriers to the commercialization of AlN-based ferroelectrics. Optimization strategies for these issues are thoroughly discussed. Advanced characterization techniques, including piezoelectric force microscopy, transmission electron microscopy, and in situ X-ray diffraction, are also highlighted for their crucial role in advancing the field. Finally, this paper concludes with a summary of the findings and provides an outlook for future research and applications. Although several review articles have discussed ferroelectric AlScN [19,24,26], this review focuses on the latest progress in the growth and ferroelectricity of AlN and its doped derivatives AlScN, AlBN, YAlN, and ScAlGaN films and provides an updated comprehensive analysis, with particular attention to the breakthroughs in enhancing ferroelectric properties in recent years, aiming to provide researchers with more cutting-edge ideas and new research directions.

2. AlN-Based Film Growth Techniques

In recent decades, various growth techniques such as MS, MBE, MOCVD, PLD, and ALD have been employed to grow AlN-based semiconductors. Each technique has distinct characteristics, with variations primarily observed in film quality, uniformity, deposition rate, and range of applications. The following section provides a detailed explanation, supported by recent studies.

2.1. Magnetron Sputtering (MS)

MS employs single metal/alloy targets, bimetallic targets, and segmented targets for reactive sputtering, utilizing metals such as Pt, Mo, and W as bottom electrodes. Alloy targets enable high deposition rates and uniform sputtering compositions, but the molding process can be challenging, and post-molding adjustments to doping content are not feasible. Dual-target co-sputtering allows for flexible control over doping concentrations and is cost-effective, though achieving uniformity on large substrates at low power remains a challenge. Segmented targets are less commonly used due to their high cost and complex maintenance requirements. Hasegawa et al. [5] deposited AlN films on (111) Nb:STO single crystals at 250 °C using reactive radio frequency (RF) magnetron sputtering with an Al target and a sputtering power of 100 W. $Al_{0.7}Sc_{0.3}N$ films were prepared at 450 °C using separate Al and Sc targets, with Al power set to 60 W and Sc power to 40 W, demonstrating polarization reversal in both films. Hayden et al. [8] deposited AlBN thin film on W electrodes using dual Al and B targets, controlling the B content (ranging from 0.02 to 0.15) by adjusting the RF power applied to the B target. These films exhibited rectangular hysteresis loops comparable to those of the $Al_{1-x}Sc_xN$ system, with polarization exceeding 125 $\mu C/cm^2$ and a coercive field greater than 5.0 MV/cm. During the sputtering process, factors such as the substrate type, sputtering power, N_2/Ar gas ratio, background gas pressure, and growth temperature significantly impact the sputtering rate, crystallinity, and ferroelectric properties [27,28]. Additionally, it has been observed that, when AlScN is deposited on a metal-polar GaN template, the lattice polarity shifts to nitrogen-polar. This polarity change occurs due to competition between the M-polar GaN template and the deposition process, which favors N-polar growth [29]. Despite challenges in achieving precise control over lattice polarity and enhancing crystallinity, magnetron sputtering remains a widely used technique for exploring new AlN-based ferroelectric materials.

2.2. Molecular Beam Epitaxy (MBE)

Compared to sputter deposition, epitaxial growth offers significant advantages in controlling phase uniformity, crystal quality, and interface integrity. Commonly used substrates include GaN, SiC, and sapphire. Wang et al. [11] utilized MBE to grow a nearly lattice-matched N-polar AlScN/GaN heterostructure with strong ferroelectric properties on a c-plane sapphire substrate. This structure demonstrated highly uniform coercive field strength (4.6 MV/cm) and residual polarization (90 $\mu C/cm^2$) across the entire wafer, with minimal degradation in performance even after 5×10^5 cycles. Casamento et al. [30] used a high-purity 4N Sc source to grow $Sc_xAl_{1-x}N/AlN$ heterostructures, achieving a Sc content of up to 0.26 and an oxygen impurity concentration ranging from 10^{19} to 10^{21} cm^{-3}. The increase in oxygen concentration was directly correlated with higher scandium content, underscoring the urgent need for Sc sources of even greater purity. In a separate study, Casamento et al. [31] grew $Al_{1-x}Sc_xN$ (x = 0.18–0.40) film, approximately 28 nm thick, on GaN substrate, achieving a smooth morphology across the entire composition range with a roughness below 0.5 nm. Compared to sputtered films, MBE significantly enhanced the crystal quality of ultra-thin AlScN, particularly at higher Sc concentrations. However, the typical purity of dopant sources such as Sc and Y (2–5 N) remains lower than

that of the Al source (6–7 N), introducing impurities that still need to be addressed for further optimization.

2.3. Metal Organic Chemical Vapor Deposition (MOCVD)

While MBE excels at growing epitaxial layers with high crystal quality and smooth interfaces, its growth rate is relatively low. In contrast, MOCVD allows for the growth of high-quality, uniform AlScN heterostructures on multiple large-diameter wafers, significantly reducing processing time. This makes MOCVD better suited to meet the demands of both fundamental research and industrial-scale production of AlN-based semiconductor materials. However, the scarcity of precursors with sufficiently high vapor pressure presents a challenge in achieving high Sc doping in AlScN. Leone et al. [32] demonstrated, for the first time, the deposition of high-quality wurtzite AlScN epitaxial layers with Sc contents up to 30% using tris-cyclopentadienyl-scandium as a Sc precursor. High-electron-mobility transistors (HEMTs) based on AlScN showed a transconductance of nearly 500 mS/mm and a drain current exceeding 1700 mA/mm, outperforming traditional AlN/GaN HEMTs [33]. Ligl et al. [34] studied the effect of growth parameters on AlScN/GaN heterostructures and found that higher growth temperature can improve surface quality. The surface roughness of samples grown at 1200 °C is as low as 0.38 nm. The V/III ratio and pressure have little effect on the layer quality. Pulsed metal organic precursors can improve surface morphology, inhibit Sc segregation and the formation of intermetallic compounds, and slightly reduce the carbon doping concentration. Leone et al. [35] found that the yttrium content doped into YAlN increases with increasing growth temperature. This may be because higher temperatures favor the decomposition of the yttrium precursor and the migration and incorporation of yttrium in the solid phase. At growth temperatures of 1100 °C and 1200 °C, cubic inclusions appear in the AlYN layer, which may be caused by excessive yttrium content. When the trimethylaluminum (TMAl) flow rate is reduced from 1.9×10^{-5} mol/min to 4.9×10^{-6} mol/min, the yttrium content increases from 20% to 30%, which is higher than the concentration shown in the literature so far. The growth temperatures for this process remain very high, ranging from 900 °C to 1200 °C, which is incompatible with CMOS processes. Further research is required to develop lower-temperature growth systems that can be integrated with a broader range of materials and substrates.

2.4. Pulsed Laser Deposition (PLD)

To date, by optimizing PLD growth conditions, high-quality III-nitride films have been successfully grown on various thermally active substrates, such as unconventional oxide substrates ($LiGaO_2$ and $MgAl_2O_4$) [36,37], metal substrates (Cu, Al, W, and Ni) [38], and Si substrates [39]. Li et al. [37] successfully grew high-quality AlN films on $MgAl_2O_4$(111) substrates at room temperature using the PLD process, solving the problem of Mg atoms diffusing from the substrate under high-temperature conditions. After annealing at 800 °C for 1 h, the interface between AlN and $MgAl_2O_4$(111) substrate remained stable. Okamoto et al. [40] attempted to grow AlN films on Mo(100), (111), and (110) substrates using PLD and found that 30°-rotated domains existed in the AlN(0001) films grown on Mo(100). While the crystal quality of AlN thin films on Mo(111) substrate is poor, single-crystal AlN thin films can be successfully grown on Mo(110) substrate. By optimizing the laser grating settings, Li et al. [41] significantly reduced the thickness nonuniformity of AlN films on Cu(111) substrates to 2.6%, which is much lower than the 10.8% of AlN films grown by conventional PLD. Ohta et al. [42] found through GIXR measurement that the roughness of the AlN/Si interface grown by PLD is only 0.5 nm, while there is a SiN_x interface layer between the AlN film grown by MOCVD and the Si substrate. Chen et al. [43] deposited a 100 nm thick $Al_{0.7}Sc_{0.3}N$ ferroelectric film via PLD, demonstrating good c-axis orientation

and excellent ferroelectric properties, with Pr > 100 μC/cm^2. In general, PLD technology overcomes the interface diffusion problem caused by MOCVD or MBE high-temperature growth and demonstrates the superiority of epitaxial growth of aluminum nitride films on a variety of substrates.

2.5. Atomic Layer Deposition (ALD)

Due to its unique self-limiting reaction, ALD enables the high-quality preparation of III-nitride semiconductors at lower temperatures (around 300 °C), making it compatible with existing CMOS processes. By adjusting the cycle ratio, the composition of alloy material can be easily tuned [44]. Oxygen is a common impurity found in AlN films. Strnad et al. [45] controlled the impurities in AlN deposition through N_2 plasma-enhanced process. By adding H_2 or NH_3 to the plasma gas, oxygen contamination was effectively eliminated without the need for plasma dose saturation and the O impurity content in the AlN film was reduced to 0.3%. By introducing plasma [46], in situ annealing [47], increasing plasma power [48], exposure time [49], etc., the reaction energy was additionally increased, which effectively improved the AlN crystal quality and provided new ideas for the ALD growth of AlN-based semiconductors. Lin et al. [4] used ALD combined with layer-by-layer in situ atomic layer annealing (ALA) to prepare 10 nm AlN at 300 °C, achieving a Pr of 3 μC/cm^2. However, considering that the Pr of AlN grown by other methods [5,8,10] is significantly higher, further verification of the ferroelectric properties of ALD-deposited AlN-based films is required.

In summary, AlN-based thin films grown by MBE and MOCVD exhibit high crystallinity and are ideal for high-performance devices, while MS and ALD may require subsequent annealing to enhance film quality. MOCVD offers the best uniformity on large-area substrates, making it more suitable for efficient industrial production. Although PLD and MBE have slower growth rates, they provide higher control precision, making them well suited for laboratory research. MS, on the other hand, is more suitable for low-cost applications. The advantages and disadvantages of each method are summarized in Table 1.

Table 1. Thin-film deposition methods and their advantages and disadvantages.

Techniques	Advantage	Disadvantage	References
MS	• High deposition rate • Suitable for large-area deposition • Applicable to most materials	• Poor film uniformity • Large film stress • Low crystal quality	[7,9,10,20,21,50–54]
MBE	• Atomic level control accuracy • Good film uniformity • Suitable for manufacturing complex heterostructures	• Low deposition rate • High equipment cost • Ultra-high vacuum environment required • Not suitable for large-area deposition	[31,55–58]
MOCVD	• High deposition rate • Good film uniformity • Suitable for large-area deposition • Mature process and equipment	• Requires high temperature environment • Expensive or toxic precursors • Reaction byproducts need to be handled • Difficult to control film composition and structure	[32–34,59]

Table 1. *Cont.*

Techniques	Advantage	Disadvantage	References
PLD	• Ability to precisely control film thickness • Suitable for deposition of various materials • High-precision replication of target components	• Poor film uniformity • Low deposition rate • High equipment cost • Prone to particle surface	[43,60,61]
ALD	• Atomic level control accuracy • Excellent film uniformity • Grow ultra-thin, uniform films • High-quality films with few defects	• Weak ferroelectricity • Very low deposition rate • Low vacuum degree • High-temperature annealing required	[4,45–49]

3. Ferroelectric Properties of AlN-Based Materials

Over the past decades, the exploration of ferroelectricity in aluminum-nitride-based materials has progressed from theoretical studies to experimental advancements. Key developments in aluminum-nitride-based ferroelectric materials are shown in Figure 2. Theoretical studies have indicated that ferroelectricity can be induced through lattice strain and elemental doping. In 2019, ferroelectric switching in Sc-doped polycrystalline AlN was demonstrated for the first time, showing a significantly lower polarization switching barrier compared to pure AlN. Building on this research, a variety of aluminum-nitride-based ferroelectric thin films have been developed, including AlBN, YAlN, and the quaternary alloy ScAlGaN. The ability to precisely control ferroelectric properties through elemental engineering marks the beginning of a new era for aluminum-nitride-based ferroelectric materials. Figure 3 summarizes the ferroelectric properties of these films. AlN itself exhibits a small Pr and a large Ec, which requires modification through element engineering. B- and Y-doped AlN show larger Pr values and significantly lower Ec, but their performance is limited by the doping concentration achievable in the current experiments. ScAlGaN, combining the benefits of multi-element doping, holds great research potential. Compared to other films, AlScN offers both a Pr >150 $\mu C/cm^2$ and an ultra-wide adjustable coercive field of 3.5–7.5 MV/cm, making it suitable for diverse application scenarios, such as high-power devices and low-power sensors. The PVD process for AlScN has already been fully industrialized, positioning ferroelectric AlScN as a promising core material for the next generation of ferroelectric devices.

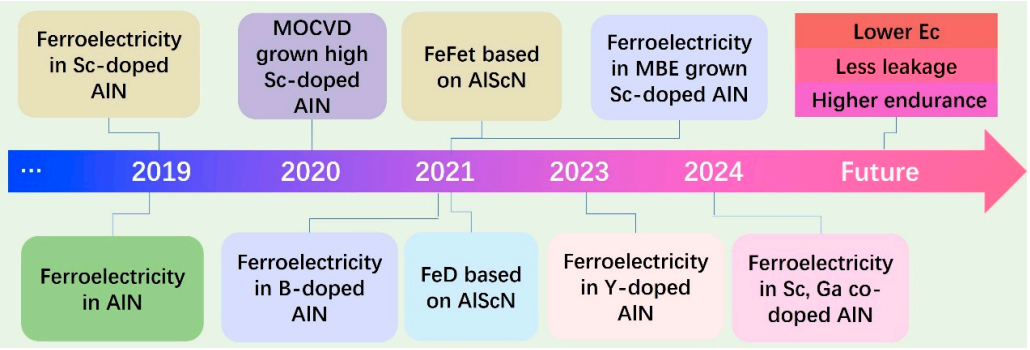

Figure 2. Historical development of aluminum-nitride-based ferroelectric materials.

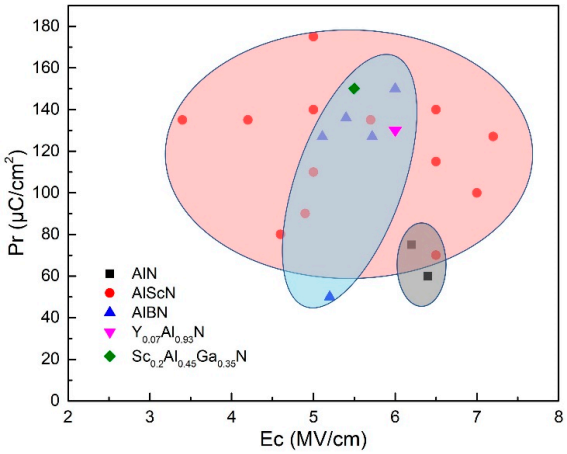

Figure 3. Pr versus Ec of AlN-based ferroelectric films. The red, blue, and gray areas represent the possible Pr-Ec ranges of AlScN, AlBN, and AlN, respectively.

The AlN data are from the ref. [5,8], AlScN from ref. [7,10,11,17,29,54,61–66], AlBN from ref. [8,67,68], YAlN from ref. [13], and ScAlGaN from ref. [14].

3.1. AlN

Wurtzite-structured AlN has two polarization states: N-polarity and M-polarity. Its structure, composed of strongly bonded tetrahedra, features a high polarization barrier, which initially led to its classification as a non-ferroelectric material. However, first-principles studies predicted two polar variants in the wurtzite structure, (0001) and (000-1), based on the relative displacement of positive and negative ions along the c-axis. These studies also suggested that applying epitaxial tensile strain on the (0001) plane could lower the barrier for polarization switching between the two variants [69,70]. In 2019, Lin et al. [4] demonstrated this effect by fully tensile straining an epitaxial AlN ultra-thin film through lattice mismatch at the AlN/GaN heterostructures interface. This reduced the polarization switching barrier and, for the first time, proved that the spontaneous polarization in AlN can switch between crystallographic directions under an electric field. AlN films with a thickness of 8–10 nm exhibited clear ferroelectricity. However, as the thickness increased to 25–38 nm, the interface strain in the AlN/GaN heterojunction was relieved through lattice misorientation, leading to weaker ferroelectricity. Figure 4a highlights that a 160 nm thick AlN film deposited at 450 °C by Hasegawa et al. [5] exhibited only local polarization switching at room temperature. In contrast, an AlN film deposited at 250 °C showed a remnant Pr exceeding 200 μC/cm^2 (Figure 4b), significantly higher than the theoretical value. This overestimation was attributed to large leakage currents, accompanied by an extraordinarily high Ec of 8 MV/cm. Hayden et al. [8] (Figure 4c), Yasuoka et al. [9] (Figure 4d), and Zhu et al. [10] also observed ferroelectric polarization in AlN films, but these films displayed only partial polarization and faced several limitations, including high leakage currents and undesirable coercive fields. Therefore, improving the ferroelectricity in AlN remains a crucial challenge. Strategies such as strain engineering, element doping (e.g., Sc, B, Y), or optimizing deposition processes are essential to enhance its performance and adapt it for practical applications.

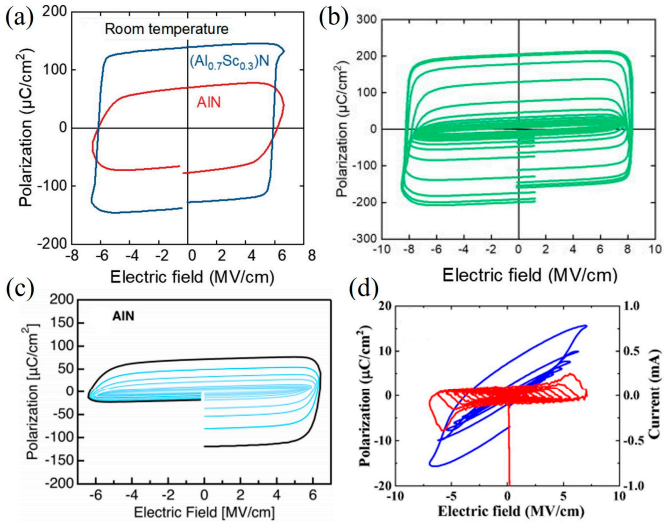

Figure 4. (**a**) P–E hysteresis loops of 450 °C deposited AlN and $Al_{0.7}Sc_{0.3}N$ measured at room temperature. (**b**) P–E hysteresis loops of 250 °C deposited AlN measured at room temperature. (**c**) Room temperature polarization hysteresis for 500 nm AlN film measured with a 200 Hz triangular wave. Nested loops are displayed at 0.1 MV/cm increments. (**d**) P–E hysteresis loops (blue) and I-V curves (red) measured at 100 kHz for AlN. (**a**,**b**) Reprinted with permission from Ref. [5]. Copyright 2023 AIP Publishing. (**c**) Reprinted with permission from Ref. [8]. Copyright 2021 American Physical Society. (**d**) Reprinted with permission from Ref. [9]. Copyright 2020 AIP Publishing.

3.2. AlScN

As early as 2010, Tasnádi et al. [6] discovered that Sc doping in AlN induces competition between the parent wurtzite phase and the metastable hexagonal phase, effectively flattening the energy landscape. This phenomenon led to a fourfold increase in the piezoelectric coefficient of AlScN alloy. Despite theoretical predictions providing valuable guidance, achieving polarization switching before film breakdown has remained a significant challenge. After nearly a decade of exploration, Fichtner et al. [7] provided the first experimental evidence in 2019 that $Al_{1-x}Sc_xN$ films exhibit ferroelectricity. They prepared $Al_{1-x}Sc_xN$ films with x = 0.27, 0.32, 0.36, 0.40, and 0.43 via reactive sputtering on 200 mm oxidized silicon wafers with AlN/Pt layers. These films demonstrated a maximum Pr exceeding 100 μC/cm^2 and exhibited an almost ideal box-shaped hysteresis loop (Figure 5a). Wang et al. [26] summarized the relationship between Pr and Ec as a function of Sc concentration (Figure 5b). With increasing Sc content, the switching barrier gradually decreases and Ec drops from 7 MV/cm to 2 MV/cm, which is attributed to in-plane tensile strain caused by the distortion of the wurtzite crystal structure. However, at higher Sc concentrations, $Al_{1-x}Sc_xN$ gradually transforms from the ferroelectric wurtzite phase to a non-ferroelectric rock-salt phase, leading to a rapid deterioration of Pr [71]. Zhang et al. [72] successfully grew high-quality AlScN single-crystal nanowires on epitaxial TiN-(111)-buffered Si (111). Differential phase contrast scanning transmission electron microscopy (DPC-STEM) revealed that each nanowire formed a single ferroelectric domain (Figure 5c). Nanowires provide an alternative approach to scaling, potentially offering benefits in reducing electrical leakage due to their reduced mosaic spread and fewer domain boundaries (or grain boundaries).

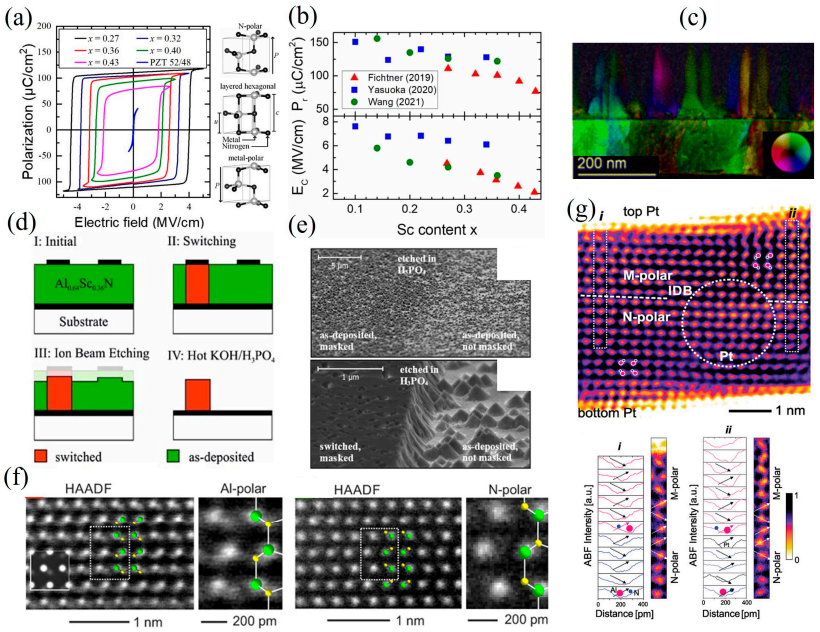

Figure 5. (**a**) P–E loop of sputtered AlScN film with Sc contents of 0.27, 0.32, 0.36, 0.40, and 0.43 as well as of PZT 52/48. To the right, the structures associated with the respective polarization states are displayed. (**b**) Evolution of remnant polarization and coercive field with Sc content of sputtered (Fichtner [7], Yasuoka [9]) and MBE-grown (Wang [64]) ScAlN thin films. (**c**) DPC STEM image of AlScN nanowires. (**d**) Schematic diagram of the experimental procedure for wet etching to determine the polarity of $Al_{0.64}Sc_{0.36}N$. (**e**) SEM images of the switching region and the deposited region before and after etching in H_3PO_4. (**f**) STEM image of AlScN film showing the cross-section of the switching region and the deposited region. (**g**) STEM image of the M- and N-domain boundaries of $Al_{0.74}Sc_{0.26}N$ and intensity profile analysis of the (Al,Sc)-N dumbbells inside the vertical single-column frames on the left (**i**) and right side (**ii**) of the grain. Profiles are drawn from left to right (see arrows) on the unfiltered image; M(-polarity) = pink, N(-polarity) = blue. (**a**,**d**,**e**) Reprinted with permission from Ref. [7]. Copyright 2019 AIP Publishing. (**b**) Reprinted with permission from Ref. [26]. Copyright 2023 IOP Publishing. (**c**) Reprinted with permission from Ref. [72]. Copyright 2024 CrystEngComm Publishing. (**f**) Reprinted with permission from Ref. [52]. Copyright 2021 AIP Publishing. (**g**) Reprinted with permission from Ref. [73]. Copyright 2023 Wiley-VCH GmbH.

Additionally, the polarity of the wurtzite unit cell exhibited anisotropy etching behavior in solutions such as KOH, TMAH, and H_3PO_4 [74]. Fichtner et al. [7] applied electrodes to a section of the film to induce polarization switching, followed by etching with H_3PO_4 for 5 min (Figure 5d). As shown in Figure 5e, the original N-polar surface was etched, leaving distinct triangular pyramid residues, whereas the M-polar surface exhibited minimal etching. The pits observed in the film may correspond to defects or inversion domain walls, providing direct evidence of polarization switching at the unit cell level. Wolff et al. [52] used spherical aberration-corrected transmission electron microscopy (Cs-TEM) to analyze cross-sections of the original and switched films. High-angle annular dark field (HAADF) imaging (Figure 5f) reveals the relative movement of N atoms with respect to the metal atoms, confirming the switching between N- and M-polarities. Schönweger et al. [73] further demonstrated the deposition of AlScN ferroelectric films less than 5 nm thick on Si, achieving polarization switching at voltages as low as ~1 V. Figure 5g shows their direct observation of inversion domain boundaries (IDBs) in a single crystal, supporting the theory of graded domain wall-driven switching in wurtzite ferroelectrics. Extensive research has been conducted on Sc-doped AlN, but challenges remain. As the Sc concentration in $Al_{1-x}Sc_xN$ increases from 0 to 0.45, the band gap decreases from 6.2 eV to 2.9 eV. In this composition range, the coercive field approaches the breakdown voltage [75].

Therefore, further exploration of alternative doping elements is essential to overcome these limitations.

3.3. AlBN

In addition to Sc doping, which reduces the polarization switching energy barrier, Hayden et al. [8] were the first to report ferroelectricity in boron-substituted AlN films. They used reactive magnetron sputtering to prepare $Al_{1-x}B_xN$ films with boron content ranging from 0 to 0.2. As shown in Figure 6a–e, when the B concentration is between 0.02 and 0.15, Pr exceeds 125 μC/cm^2. However, at a concentration greater than 0.15, the ferroelectric properties deteriorate and eventually vanish. This decline is likely caused by the BN substitution driving the structure toward a centrosymmetric hexagonal phase or substantial AOG surface coverage hindering polarization switching in the underlying c-axis-oriented material. Figure 6f–i further shows that, as boron content increases, both Ec and Pr decrease continuously. This trend is similar to the $Al_{1-x}Sc_xN$ ferroelectric system, although the tunable window for AlBN is narrower, with Ec decreasing by only 10%. Both the a and c lattice parameters decrease monotonically, leading to a reduction in unit cell volume, which can be attributed to the smaller ionic radius of boron compared to aluminum. Unlike $Al_{1-x}Sc_xN$, where increasing Sc content causes the c-axis to contract and the basal plane to expand, the c/a ratio remains constant at 1.60. In contrast, the c/a ratio for $Al_{1-x}Sc_xN$ drops to approximately 1.3 at x = 0.46 [76]. Notably, AlBN maintains a bandgap greater than 4.9 eV across the experimentally accessible composition range, without introducing significant leakage current.

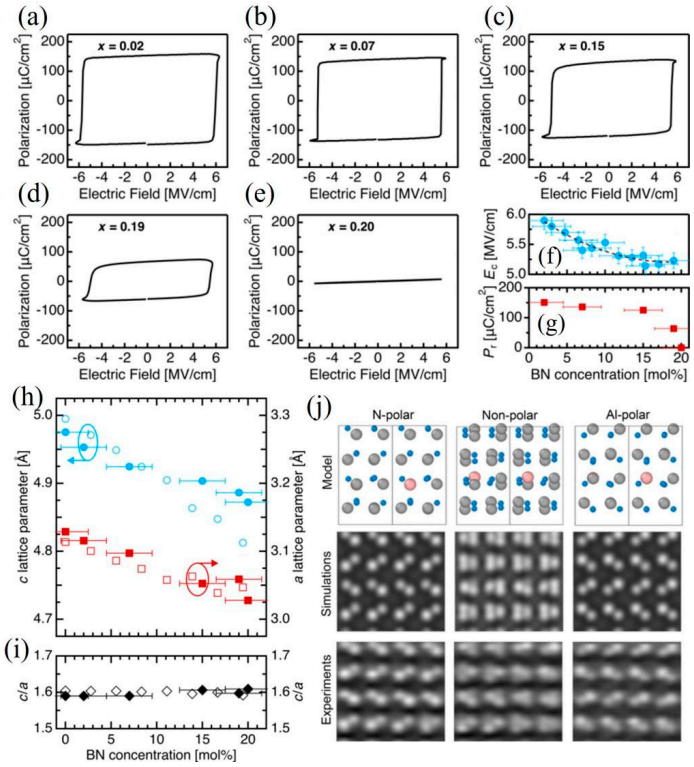

Figure 6. (**a**–**e**) Polarization hysteresis for 500 nm $Al_{1-x}B_xN$ films with x = 0.00, 0.02, 0.07, 0.15, 0.19, 0.20. (**f**) Dependence of Ec on B concentration. (**g**) Dependence of Pr on B concentration. (**h**) $Al_{1-x}B_xN$ c and a lattice parameters as a function of B concentration, as determined by in- and out-of-plane XRD measurements (filled markers) and first-principles calculations (open markers). (**i**) c/a parameters of $Al_{1-x}B_xN$. Error in the measured lattice parameters is smaller than the size of the markers. (**j**) Atomic model, STEM image simulation, and experimental images of N polar, nonpolar, and Al polar states of AlBN. (**a**–**i**) Reprinted with permission from Ref. [8]. Copyright 2021 American Physical Society. (**j**) Reprinted with permission from Ref. [77]. Copyright 2023 AAAS.

Sebastian et al. [77] used STEM in differentiated differential phase contrast (dDPC) mode to observe in situ polarization reversal in an $Al_{0.94}B_{0.06}N$ film. As shown in Figure 6j, the reversal process transitions from initial N polarity, through a transient nonpolar intermediate state, to the final Al polarity. The simulated images align well with the STEM images at different stages of the switching process. This understanding of macroscopic and atomic-scale in situ polarization switching in AlN-based ferroelectric materials offers valuable guidance for future research on other wurtzite-structured ferroelectric materials, such as ZnMgO.

3.4. YAlN

Yttrium (Y), which has an electron shell structure similar to Sc, has also been proposed as a doping element in AlN, leading to lattice softening and a significant enhancement in the material's piezoelectric response. Mayrhofer et al. [78] predict that, at 50% Y content, YAlN can surpass the piezoelectric coefficient of AlScN, achieving a maximum d_{33} of 35 pC/N. Both theoretical studies and early experimental results indicate that YAlN can maintain a stable single wurtzite phase even at Y contents as high as 75%, whereas Sc concentrations exceeding 40% in AlScN result in partial transformation into a non-ferroelectric rock-salt phase [79–81]. As a substitute for scandium, a $Y_{0.09}Al_{0.91}N$ thin film was sputtered on a (100) silicon substrate using an $Al_{0.85}Y_{0.15}$ alloy target, achieving a piezoelectric coefficient d_{33} of 7.79 pC/N, which closely aligns with the theoretical prediction of 6.9 pC/N [82]. Wang et al. [13] were the first to report ferroelectric switching in a wurtzite-phase single-crystal YAlN film grown on GaN using MBE. The epitaxially grown YAlN film, with a Y content of 0.07, obtained a coercive force field of 6 MV/cm and a remnant polarization of up to 130 μC/cm^2 (Figure 7a,b). Although theoretical predictions highlight the unlimited potential of YAlN, current experiments have only found ferroelectricity at low Y concentrations. Future research should focus on growing high-quality, highly Y-doped AlN films to fully explore their ferroelectric properties.

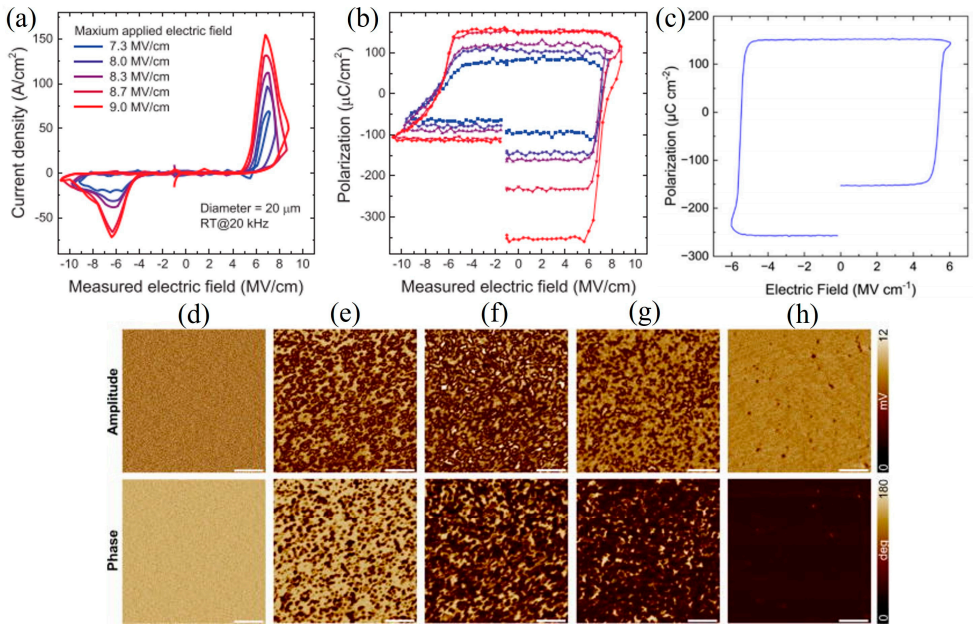

Figure 7. J-E loop (**a**) and the corresponding P-E loop (**b**) of YAlN film, with maximum bias voltage of 7.3–9.0 MV/cm. (**c**) Representative P–E loop for the $Sc_{0.2}Al_{0.45}Ga_{0.35}N$ film. (**d**–**h**) PFM amplitude and phase images of $Sc_{0.2}Al_{0.45}Ga_{0.35}N$ film. The nucleation and growth of polarity inversion domains are clearly evidenced. The scale bars represent 1 μm. (**a**,**b**) Reprinted with permission from Ref. [13]. Copyright 2023 AIP Publishing. (**c**–**h**) Reprinted with permission from Ref. [14]. Copyright 2024 AIP Publishing.

3.5. ScAlGaN

Currently, MBE mainly focuses on the N-rich growth mechanism to prevent the formation of undesirable intermetallic compounds, such as Sc-Al and perovskites like Sc_3AlN. However, this growth mode causes $Sc_xAl_{1-x}N$ to develop a granular surface, where local trap states form at the granular interfaces. These trap states limit the transport characteristics of mobile carriers, ultimately leading to degradation in device performance [31,58,83]. Wang et al. [84] explored the metal-rich growth mechanism and found that the film quality of epitaxially grown AlScN can be significantly improved by alloying with Ga. The oxygen impurity content in ScAlGaN was found to be three to four orders of magnitude lower than in AlScN grown on an AlN template, indicating enhanced migration ability of the colliding atoms during growth.

The quaternary alloy $Sc_xAl_yGa_{1-x-y}N$ offers a tunable bridge between $Sc_xAl_{1-x}N$ and $Sc_xGa_{1-x}N$. Yang et al. [14] grew single-crystal $Sc_{0.2}Al_{0.45}Ga_{0.35}N$ on Mo using plasma-assisted MBE and elucidated its ferroelectric switching behavior. Their results revealed a coercive field of 5.5 MV/cm and a high remanent polarization of 150 $\mu C/cm^2$ (Figure 7c). Piezoelectric force microscopy (PFM) studies further showed that the polarization reversal in $Sc_xAl_yGa_{1-x-y}N$ follows a domain nucleation and growth pattern (Figure 7d–h). This ferroelectric quaternary alloy significantly broadens the tunability of band gap, lattice parameters, and piezoelectric constants, making it highly versatile for applications in advanced electronic, optoelectronic, and acoustic devices and systems.

4. Strategies for Improving Ferroelectricity in AlN-Based Materials

AlN-based ferroelectric thin films exhibit significant application potential, but several challenges remain to be addressed. Taking AlScN, the most representative extensively studied and deeply explored material, as an example, we can highlight key issues. For example, the Ec of AlScN is relatively high, which implies that FeRAM applications would require larger operating voltages, even when the film is scaled down to ultra-thin thickness. Additionally, as the external electric field approaches Ec, the leakage current in AlScN increases, potentially due to N vacancies. Durability is another critical factor; despite improvements in crystal quality that have extended the lifetime of AlScN from approximately 10^5 cycles to over 10^7 cycles, it still does not meet the stringent requirements for commercial applications [85]. To solve these issues, researchers have proposed various optimization methods, including stress regulation, annealing, stacking structure design, etc. The applicability and effectiveness of these improvement strategies will be discussed in detail below.

4.1. Effects of Stress

High Ec is a double-edged sword for device design. While a high Ec is beneficial for long-term data retention and large memory windows, the relatively high voltage required for ferroelectric switching accelerates material degradation and reduces the cycle life of $Al_{1-x}Sc_xN$. Increasing the Sc alloying ratio can effectively lower Ec; however, the strong thermodynamic driving force of phase separation and the reduction in band gap lead to material quality degradation and higher leakage currents. Recent studies have found that the strain sensitivity of the switching energy barrier in wurtzite ferroelectrics is an order of magnitude larger than the spontaneous polarization (Figure 8a,b) [86]. There is a clear correlation between stress and Ec in AlScN, where increasing tensile stress reduces Ec without compromising material quality as severely as high Sc alloying. Practical methods for stress regulation include thermal straining, adjusting deposition parameters, and substrate strain engineering.

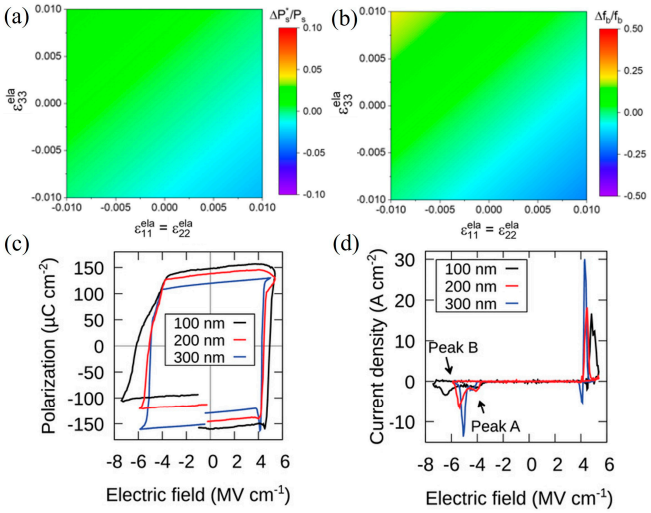

Figure 8. (**a**) Normalized spontaneous polarization map for $Al_{0.8}Sc_{0.2}N$ under ±1% of elastic strain. (**b**) Normalized free energy barrier diagram of $Al_{0.8}Sc_{0.2}N$ under ±1% elastic strain. (**c**) Dynamic leakage current compensation (DLCC) (1 kHz) P–E loop of $Al_{0.72}Sc_{0.28}N$ film. (**d**) Corresponding DLCC (1 kHz) J–E curve of $Al_{0.72}Sc_{0.28}N$ film. (**a**,**b**) Reprinted with permission from Ref. [86]. Copyright 2022 AIP Publishing. (**c**,**d**) Reprinted with permission from Ref. [29]. Copyright 2022 Wiley-VCH GmbH.

Yasuoka et al. [65] demonstrated that the c/a ratio of AlScN films increases when deposition occurs at elevated temperatures and cools to room temperature, a result attributed to thermal strain. Since the thermal expansion coefficient of $Al_{0.78}Sc_{0.22}N$ (6.2×10^{-6}/°C) is greater than Si, in-plane tensile strain develops during cooling. They further investigated 145 nm thick $Al_{0.8}Sc_{0.2}N$ films deposited on 0.5 mm thick fused silica (SiO_2), (100)Si, (0001)Al_2O_3, and (100)MgO, with thermal expansion coefficients of 0.54, 4.0, 7.7, and 13.5×10^{-6}/°C, respectively [54]. When sputtering occurs at room temperature, films deposited on fused silica and Si substrates undergo in-plane tension stress, while those on Al_2O_3 and MgO substrates undergo in-plane compression stress. Consequently, Ec decreases from 7.2 MV/cm to 6.6 MV/cm as the stress transforms from compressive to tensile. Ryoo et al. [27] systematically studied the structure and ferroelectric switching behavior of $Al_{0.7}Sc_{0.3}N$ films on TiN electrodes under varying deposition parameters and compressive stress caused by atomic shot peening. Due to high tensile stress at grain boundaries, increasing the power from 300 W to 600 W was insufficient to induce compressive stress [87]. As nitrogen content increases, film stress changes from tensile to compressive. The increase in sputtering gas pressure reduces the atomic energy and the atomic shot peening effect, resulting in a shift of in-plane stress from compressive to tensile. The change in stress values from 0 to 400 °C can be attributed to thermal stress and the shot-peening relaxation effect at high temperatures [88]. The thermal expansion coefficient of $Al_{0.7}Sc_{0.3}N$ is higher than Si, which causes the film to shrink more significantly when cooled at higher deposition temperatures, thereby generating higher tensile stress. Among these four process parameters, deposition temperature has the most significant impact on stress but, in general, Ec has a maximum change window of 10%.

As previously mentioned, lattice-mismatched epitaxial tensile strain reduces the polarization-switching energy barrier of AlN. In the case of epitaxial growth, the thickness range of strain action is also worthy of attention. Schönweger et al. [29] found that $Al_{0.72}Sc_{0.28}N$ films up to 40 nm remain fully compressively strained on GaN, whereas films between 40 and 300 nm exhibited a combination of fully strained and more relaxed volumes. Multiple strain states cause the ferroelectric displacement current to split into different peaks (Figure 8c,d). Peak B with a higher switching voltage corresponds to polarization

switching in the strained region near the GaN interface, while peak A with a lower voltage is responsible for switching to a more relaxed region. In addition, Islam et al. [89] found that, compared with compressively stressed $Al_{0.72}Sc_{0.28}N$ films grown directly on GaN/Al_2O_3, epitaxial films relaxed on 10 nm epitaxial Pt have lower correction fields, leakage currents, and more symmetrical ferroelectric responses.

Future advancements in AlScN films will hinge on effectively and controllably regulating stress. Inspired by the study of group III nitride systems, Ec can be fine-tuned through various strain mechanisms, including epitaxial mismatch strain, thermal strain induced by buffer electrodes and substrates, sputtering gas partial pressure, sputtering power, growth temperature, and thermal annealing energy differences. Combining these strategies is expected to fully exploit the potential of aluminum-nitride-based ferroelectrics, overcome the limitations associated with high coercive fields, and promote their integration into low-power devices.

4.2. Leakage Current and Improvement

In the study of $Al_{1-x}Sc_xN$ films as piezoelectric materials, reports of large leakage currents are relatively scarce, likely due to the limited electric field range in piezoelectric applications. The empirical relationship for the band gap (Eg) of $Al_{1-x}Sc_xN$ films is given by $Eg(x) = -9.5x + 6.2$ (eV), $(0 < x < 0.34)$ [75]. As the Sc concentration x ranges from 0 to 0.3, the band gap of $Al_{1-x}Sc_xN$ films spans from 6.2 to 3.4 eV, categorizing it as a wide-bandgap insulator. However, in ferroelectric applications, the leakage current in $Al_{1-x}Sc_xN$ films is unexpectedly high and further increases with higher Sc concentrations, posing a significant challenge to the durability and reliability of devices.

Li et al. [43] conducted an in-depth study into the source and cycling behavior of leakage current in 100 nm $Al_{0.7}Sc_{0.3}N$-based FeRAM through experiments and calculations. They found that the large leakage current may come from positively charged nitrogen vacancies [61], aligning with the trap-assisted Poole–Frenkel emission model. Cycling studies showed that the leakage current only increased significantly under bipolar cycling conditions that exceeded the coercive field. This was attributed to the reduction in trap energy levels after continuous bipolar cycling. Further studies on ultra-thin films (50 nm) demonstrated that, in scaled-down $Al_{1-x}Sc_xN$, the large leakage was primarily driven by defect concentration rather than trap energy levels [90]. To elucidate the microscopic mechanism of leakage current, Li et al. [60] analyzed cross-sectional transmission electron microscopy (TEM) images of uncycled devices and bipolar cycled devices with pulse amplitudes exceeding Ec. In the initial state, 11 complete grains were visible, which split into 16 grains after continuous bipolar cycling. This reduction in average grain size and the significant decrease in the proportion of large grains indicate that, during continuous polarization switching, grain fragmentation occurs and more defects may be generated at the grain boundaries, leading to ferroelectric degradation and increased leakage current.

To suppress the leakage current, Liu et al. [91] annealed the AlScN film in a pure N_2 atmosphere for 1 h, observing improved crystal quality with increasing annealing temperature. After annealing at 400 °C, the leakage current of the AlScN film can be reduced by 4 orders of magnitude (Figure 9a). In addition, the ellipsoidal P−E loop caused by the leakage current becomes a square (Figure 9b). Compared with the initial film (Figure 9c), the energy provided by annealing promotes the evolution of AOG toward the c-axis orientation, as confirmed by the TEM image of Figure 9d. However, higher annealing temperatures increase the risk of oxygen incorporation. At 800 °C, oxygen content at AlScN/Ti electrode interface more than doubles, forming an oxide layer approximately 21.4 nm thick (Figure 9e). This oxide layer inhibits the relative displacement of metal and nitrogen atoms in AlScN, resulting in a sharp drop in residual polarization [92]. This

experimental scheme highlights the need to balance annealing temperature to optimize ferroelectric performance.

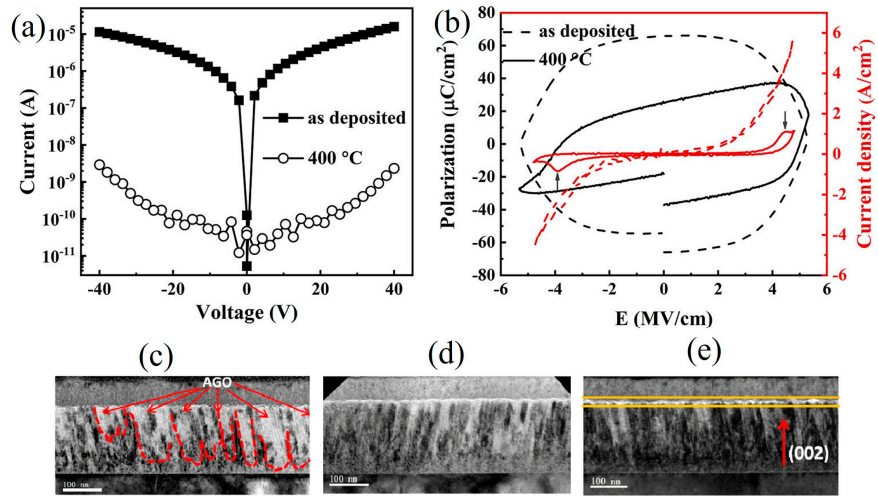

Figure 9. Leakage current (**a**) and P−E/J−E loops (**b**) of AlScN film before and after 400 °C annealing. (**c**–**e**) Cross-sections of original, 400 °C, and 800 °C annealed AlScN. (**a**–**e**) Reprinted with permission from Ref. [91]. Copyright 2024 American Chemical Society.

Zheng et al. [93] found that, compared to single-layer $Al_{0.72}Sc_{0.28}N$ and $Al_{0.64}Sc_{0.36}N$, the deposited multilayer film has lower leakage current and enhanced breakdown field strength because the propagation of the electric tree is deflected by the multilayer interface or slowed down by the relative compressive stress in the alternating layers. In addition, further reducing the thickness of $Al_{0.72}Sc_{0.28}N$/epi-Pt/GaN epitaxial Pt from 100 nm to 10 nm with reduced surface roughness can significantly improve the leakage current performance [89]. The leakage current is also closely related to the film stress. The experimental results show that the leakage current is unevenly distributed across the wafer. The central area, characterized by the least compressive stress, exhibits the lowest leakage current, while the edge region shows higher leakage values [94]. Furthermore, DFT calculations also show that the leakage current is more sensitive to compressive stress than tensile stress, and the minimum leakage current can be obtained under neutral in-plane stress [95], and a higher nitrogen flow rate may be beneficial to this [96,97].

Therefore, strategies such as reducing dislocation density, nitrogen annealing, depositing multilayer or concentration gradient films, utilizing epitaxial electrode buffer layers, and minimizing compressive stress offer promising pathways to suppress leakage current. A comprehensive understanding of these approaches is necessary to overcome the high leakage current in nitride ferroelectric devices, improve device performance, and expand their applications in advanced electronic systems.

4.3. Fatigue and Enhancement

The durability of AlScN film remains relatively low, with most studies reporting a decrease in Pr after about 10^4–10^5 cycles [11,64], whereas HfZrO-based FeRAM has achieved a cycle life of up to 10^{12} cycles [98]. Therefore, further investigation into the underlying causes of fatigue in AlScN is essential. Wang et al. [99] prepared $Al_{0.65}Sc_{0.35}N$ films under nitrogen-rich conditions, achieving a cycle life exceeding 2×10^7, which surpasses the performance of similar materials reported in the literature [53,100–103]. To explore the microscopic fatigue mechanism, in situ electron microscopy was used to dynamically observe the composition and distribution of nitrogen and oxygen elements in AlScN films during ferroelectric cycling. As shown in Figure 10a,b, TEM and EDS analyses provide solid evidence that prolonged cycling causes oxygen to penetrate from

the electrode interface along the grain boundary and diffuse into various regions in the film. This phenomenon is particularly pronounced near the air-exposed edges of the electrode (Figure 10c), resulting in a large amount of nitrogen loss in the upper part of the film and oxidation and amorphization of the AlScN film. The expansion of the non-ferroelectric interface dielectric layer during continuous electric field cycling induces charge capture and thus damages the polarization switch. This study reveals one of the key mechanisms behind the limited endurance of AlScN and provides valuable insights for future experiments aimed at mitigating fatigue.

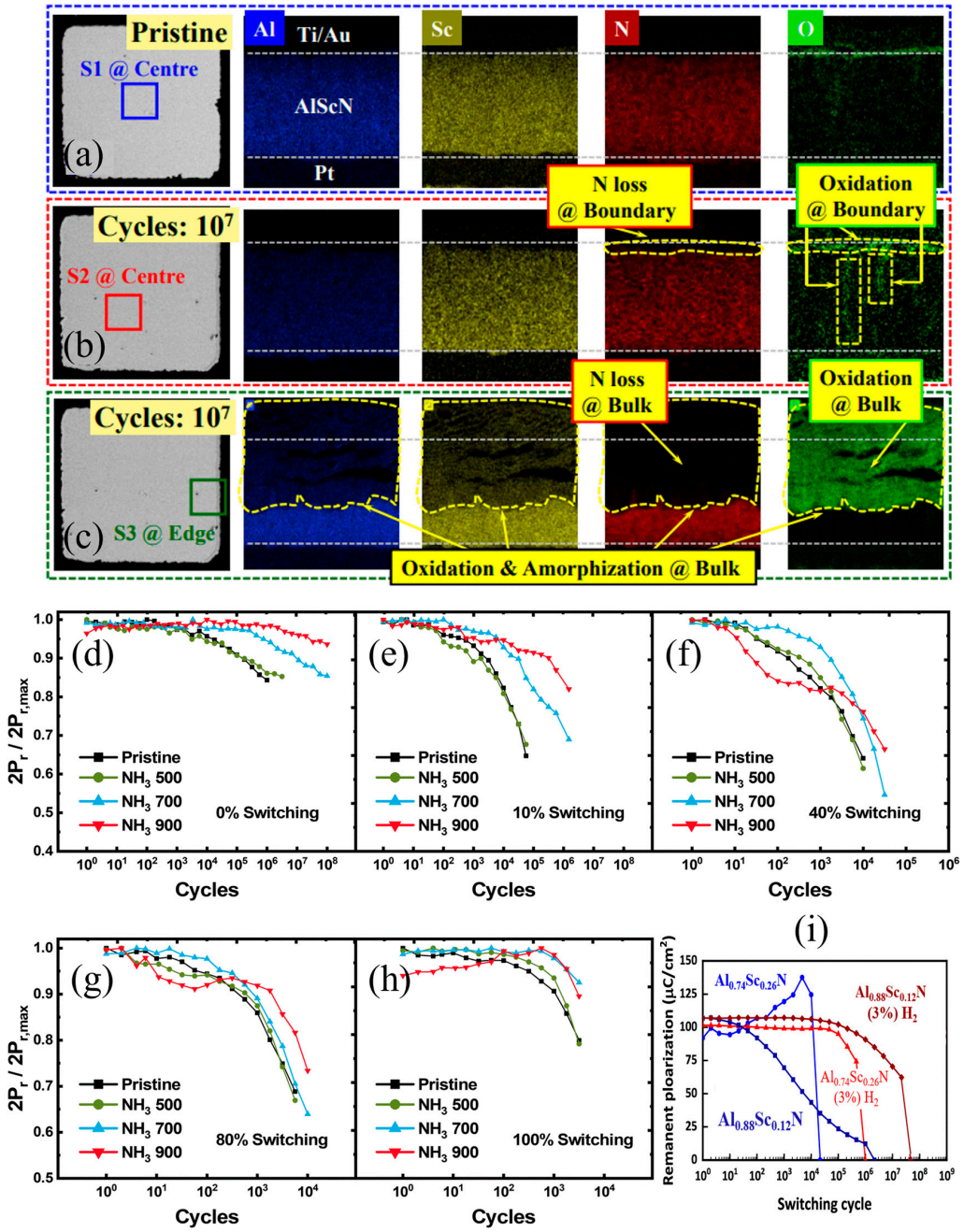

Figure 10. TEM and EDS analysis of three samples: (**a**) the center area of the original device, (**b**) the center area of the device after 1×10^7 cycles, (**c**) the edge area. (**d**–**h**) Fatigue characteristics of samples annealed with different switching ratios. (**i**) Durability cycles of high Sc and low Sc samples before and after H_2 improvement. (**a**–**c**) Reprinted with permission from Ref. [99]. License CC BY-NC-ND. (**d**–**h**) Reprinted with permission from Ref. [104]. Copyright 2023 Royal Society of Chemistry. (**i**) Reprinted with permission from Ref. [105]. Copyright 2024 IOP Publishing.

Kim et al. [100] proposed that the thickening of the non-ferroelectric layer during high-electric-field cycling leads to depolarization effects and accompanying fatigue. During low-voltage cycling, the increase in domain wall density induces domain wall pinning, exacerbating fatigue, with film defects accelerating this process. To address this, they annealed AlScN film in an NH_3 atmosphere for 30 s to reduce the defects and oxygen impurities [104]. Experimental results at various switching ratios and annealing temperatures are shown in Figure 10d–h. When the switching ratio is 0%, NH_3 annealing improved the durability by over two orders of magnitude. However, as the switching ratio increases, the fatigue mitigation effect diminishes. As the switching ratio is 40%, 80%, and 100%, AlScN after NH_3 annealing at 900 °C exhibits a phenomenon of initial wake-up followed by fatigue, though the underlying reasons remain unclear. Introducing H_2 during the sputtering process can also suppress fatigue [105]. Adding 3% H_2 effectively suppressed the wake-up effect in high-Sc films, improving durability by two orders of magnitude. The fatigue effect in low-Sc film was greatly weakened, with cycle numbers dramatically increasing to 2×10^7 cycles. This demonstrates that H_2 can effectively remove oxygen impurities from Sc and Al atoms. Besides the residual oxygen in the chamber, another potential source of oxygen impurities could be the oxygen atoms present in the AlSc target.

The role of the top electrode is also critical but often overlooked. The film with a 100 nm thick Pt top electrode can endure about 10^4 bipolar cycles before dielectric breakdown, while the film with a 1000 nm W top electrode can survive about 10^5 bipolar cycles. Additionally, incorporating an SU8 field plate on the top electrode increases the number of cycles to ~10^6 times [106].

To improve durability, it is essential to protect device packaging to prevent direct contact between the electrode/dielectric layers and the atmosphere. Using high-purity targets or sources is crucial, along with minimizing impurities and defects during and after sputtering. Additionally, optimizing electrode design can effectively reduce fatigue, enhancing the long-term reliability of AlScN-based devices.

4.4. Stability

Although other ferroelectric materials may exhibit good thermal stability, such as the common hafnium-based ferroelectrics and perovskite ferroelectric oxides, which can withstand temperatures below 600 °C, none reported to date can match the exceptional thermal stability of $Al_{1-x}Sc_xN$ above 1100 °C [24]. This characteristic opens up significant opportunities for its applications in sensing, electronics, and energy conversion in high-temperature environments.

The temperature dependence coefficient of frequency (TCf) is a crucial parameter for Micro-Electro-Mechanical Systems (MEMS) devices, as it reflects their performance stability over a range of temperatures. Sui et al. [107] studied AlScN/SiC thin-film micromechanical resonant transducers operating at high temperatures up to 600 °C. The average TCf of the first resonant mode of the 250 μm diameter resonator is less than 1 ppm/K between 25 and 200 °C and −16 ppm/K between 200 and 600 °C, with better temperature stability than MEMS resonators based on AlN or 3C-SiC [108,109]. Zheng et al. [66] fabricated an $Al_{0.8}Sc_{0.2}N$/GaN/sapphire surface acoustic wave (SAW) resonator, and the TCf of the R mode and S mode was tested up to 600 K, showing a stable value of about −30 ppm/K.

Data retention over time is a critical characteristic of NVM. Zhu et al. [68] sputtered $Al_{0.93}B_{0.07}N$ thin films onto W/Al_2O_3 substrates to construct metal–ferroelectric–metal stacks and measured retention rates at baking temperatures ranging from room temperature to 200 °C. Figure 11a,b show the retention in the same state (SS) and opposite state (OS). After heating at 100 °C and 150 °C for 500 h, polarization losses were negligible. Even after baking at 200 °C for 1000 h, the signal margin exceeds 200 μC/cm^2, and it is estimated that

the OS retention rate is 82% after baking at 200 °C for 10 years. In comparison, PZT-based FeRAM has a signal margin of less than 10 μC/cm^2 after baking [110]. Pradhan et al. [111] demonstrated an NVM device based on a 45 nm thick $Al_{0.68}Sc_{0.32}N$ ferroelectric diode. Figure 11c,d shows that the device can operate stably with clear ferroelectric switching up to 600 °C with distinguishable On and Off states. At 500 °C, 1 million read cycles were shown with a stable on/off ratio of more than 6 h. The diode operates at a voltage below 15 V at 600 °C, making it well matched and compatible with high-temperature logic technology based on silicon carbide (SiC). These findings underscore the remarkable thermal stability and performance of $Al_{1-x}Sc_xN$-based devices, positioning them as promising candidates for advanced high-temperature electronics and NVM applications.

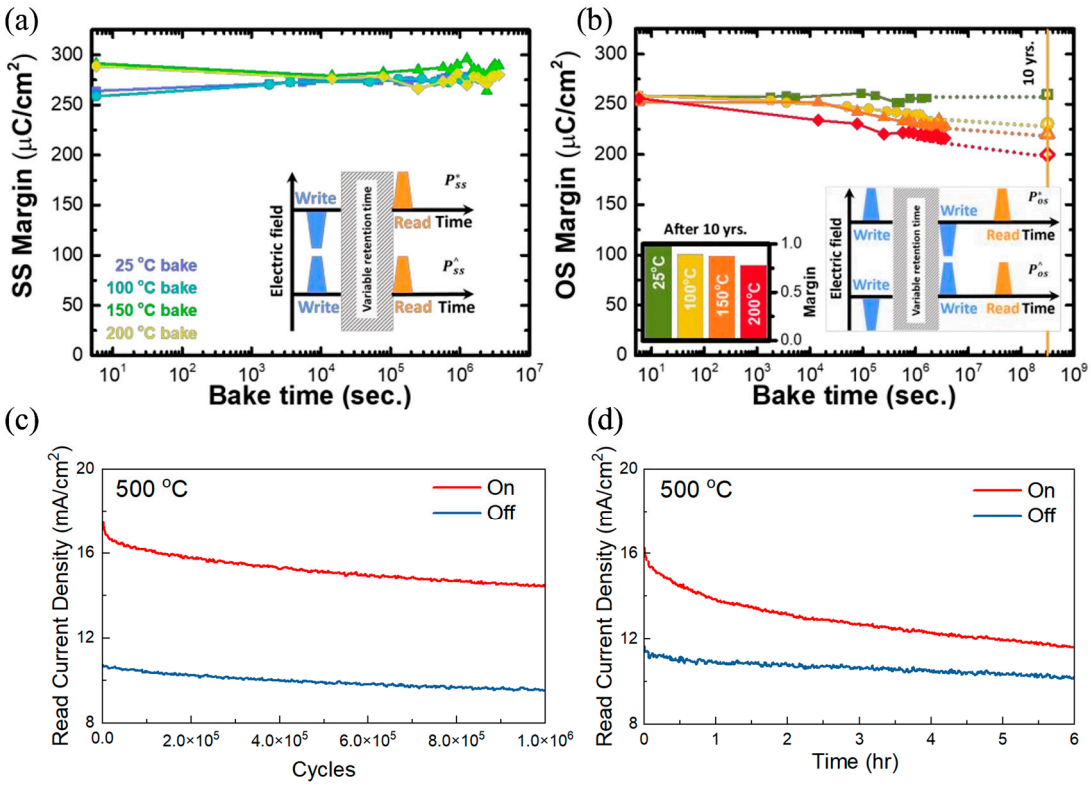

Figure 11. Variation in the same-state polarization margin (**a**) and opposite-state polarization margin (**b**) of $Al_{0.93}B_{0.07}N$ film with baking time from room temperature to 200 °C. Read cycle (**c**) and retention behavior (**d**) of $Al_{0.68}Sc_{0.32}N$ ferroelectric diode at 5 V and 500 °C. (**a**,**b**) Reprinted with permission from Ref. [68]. Copyright 2023 AIP Publishing. (**c**,**d**) Reprinted with permission from Ref. [111]. License CC BY.

AlScN demonstrates great potential for high-temperature applications, making the study of its structure at elevated temperatures crucial. Weak signs of degradation can be observed in the 0002 reflection region of $Al_{0.73}Sc_{0.27}N$ films (about 10%) after annealing above 800 °C, which may be attributed to the formation of small grains and Sc-rich $AlScO_x$ layer on the film surface [112]. The formation of grains may be affected by the presence of hydrocarbons, and the Sc-rich $AlScO_x$ is caused by the diffusion of Sc and Al through the native oxide layer, reacting with residual oxygen in the vacuum chamber. In situ high-temperature XRD has provided detailed insights into the structural stability of $Al_{1-x}Sc_xN$ at 100–1100 °C. The results revealed a monotonic lattice expansion, consistent with thermal expansion expectations while maintaining a constant c/a ratio and preserving a single wurtzite structure [51]. However, high temperature also revealed the structural degradation of AlScN film and the irreversible anomalous nonlinear thermal expansion, that is, the transition from the initial expansion state to a rapid expansion state at high temperatures.

The thermal expansion behavior is contributed by the thermal activation, migration, and solidification of the intrinsic defect structure and the external oxygen impurities [113]. Additionally, high Sc doping destabilizes the AlN lattice due to its larger cation size and structural preference for octahedral co-ordination, inducing higher defect density. Sc has a strong affinity for oxygen [30], and the intrinsic oxygen impurities of AlScN films are also proportional to the Sc content. At high temperatures around 800 °C, oxygen can diffuse into the $Al_{1-x}Sc_xN$ material through defects and grain boundaries, interacting with thermally activated defect sites and promoting further lattice expansion. This process can generate significant stress in adjacent layers, potentially leading to device failure or reliability issues.

To mitigate these risks, minimizing defects within $Al_{1-x}Sc_xN$ is crucial. Measures such as using temperature-resistant electrodes (e.g., Mo or NbN) to protect the top layer and preventing oxidation of functional layers are essential. The defect density of the material must also be carefully considered when operating AlScN films at high temperatures. Further investigation of defect structures using advanced techniques, such as positron annihilation spectroscopy, is necessary to gain a deeper understanding of these mechanisms. Such insights are particularly significant for integrating AlScN layers into advanced sandwich structures, such as ferroelectric field-effect transistor or ferroelectric tunnel junctions, where thermal stability and reliability are paramount.

5. Applications in Electronics and Photonics

HEMTs using epitaxial AlN-based films as functional barrier layers are a major advance in high-power and high-frequency electronic devices. Inserting a 2 nm AlN interlayer into an epitaxial AlScN/GaN structure increases the room temperature mobility by more than five times and the mobility at 10 K by more than 20 times to ~6980 cm^2/Vs [114]. HEMTs based on $Y_{0.07}Al_{0.93}N$/AlN/GaN heterostructures have a sheet electron concentration of 4.2×10^{13} cm^2 and a sheet resistance as low as 148 Ω/□, which brings significant performance improvements to this type of device, such as high current density, transconductance, output power, and efficiency [115]. Doping has significantly improved the ferroelectric properties of AlN, especially under high frequency, high temperature, and high voltage environments, showing stronger stability and adjustable polarization characteristics, and has great application potential in the field of ferroelectric memory, especially in devices such as FeFET, FeD, and ferroelectric tunnel junction (FTJ). Liu et al. [21] developed a 20 nm $Al_{0.64}Sc_{0.36}N$-based metal–ferroelectric–metal (MFM) diode that demonstrated a 10^5 rectification ratio and exhibited memristive behavior with an on/off ratio of 5×10^4 between low-resistance and high-resistance states. Liu et al. [20] also designed a FeFET composed of 100 nm ferroelectric $Al_{0.71}Sc_{0.29}N$ and two-dimensional MoS_2, which achieved an on/off drain-source resistance ratio of more than 10^5 under a ferroelectric-induced memory window of 30–40 V and showed no significant attenuation in 10^4 cycles and a retention time of $<10^5$ seconds. These devices perform well in repeated programing and processes, with excellent durability and excellent retention characteristics. They are ideal for advanced memories in future energy-saving and scalable electronic devices.

AlScN's CMOS compatibility can promote the large-scale production of integrated photonic modulators and, compared with intrinsic AlN, it has a higher piezoelectric effect and a larger optical second-order polarizability, indicating the possibility of efficient modulation, and is considered to be a new platform for future integrated photonics [116]. Huang et al. [117] demonstrated the acousto-optic modulation in silicon waveguides of piezoelectric $Al_{0.6}Sc_{0.4}N$ films deposited on a silicon-on-insulator platform. By designing a compact spiral waveguide structure with multiple interaction segments, the acousto-optic device can achieve broadband acousto-optic modulation and narrowband microwave photon filtering. Friedmanet al. [118] partially physically etched $Al_{0.70}$ $Sc_{0.30}N$ to make a

waveguide and extracted a propagation loss as low as 1.6 ± 0.3 dB/cm at a wavelength of around 1550 nm. The highest quality factor of the resonator is greater than 8.7×10^4, and the propagation loss value is lower than any previously published value, indicating that this material can be widely used in optical modulators without significant loss. This result paves the way for low-loss integrated AlScN photonic applications. Mondal et al. [119] explored the unique optoelectronic properties of ultra-wide-bandgap AlScN and demonstrated for the first time a high-performance ferroelectric self-powered deep ultraviolet photodetector based on epitaxially grown AlScN thin films. At an extremely low light intensity of 0.12 mW/cm^2, the responsivity reached 15 mA/W and the detectivity was 1.2×10^{11} Jones, showing no wake-up, fast response time (<0.06 s) and stability, and excellent suppression of UV-A and visible light illumination. Finally, due to its combination of multiple properties, including high piezoelectricity, ferroelectricity, high Curie temperature, ultra-wide bandgap, and high temperature stability, ScAlN also has considerable advantages in ultraviolet photodetectors [119], electro-optic phase shifters [116], acousto-optic modulators [117,120,121], and other applications.

6. Summary and Prospect

The discovery of AlN-based ferroelectrics marks a significant milestone in the field of ferroelectric materials. By combining the exceptional properties of wide-bandgap semiconductors and ferroelectric materials, AlN-based ferroelectrics exhibit the potential to operate under high-frequency, high-temperature, and low-power consumption conditions. This breakthrough not only advances the development of new ferroelectric materials but also paves the way for innovative applications in future electronic technologies. This review summarizes the advantages and limitations of various growth technologies for preparing AlN-based semiconductors, highlighting their suitability for specific scenarios. Additionally, we compile evidence of ferroelectricity in AlN doped with various elements and provide a comparative analysis of their ferroelectric properties. Key aspects such as the coercive field, leakage current, fatigue, thermal stability, and corresponding improvement strategies for ferroelectric films are also discussed. Finally, the applications of AlN-based materials in electronics and photonics are briefly reviewed.

Despite notable progress in the growth technology of AlN-based ferroelectric thin films, several challenges remain, with issues such as lattice mismatch, stress control, and achieving high-quality single-crystal growth persist. Producing high-quality films at nanometer or atomic scales to achieve lower operating voltages is particularly challenging, as reducing film thickness often introduces significant defects. This necessitates the development of more advanced fabrication techniques. Furthermore, the issue of high leakage current, a critical barrier to industrialization, must be urgently addressed. This challenge is attributed to factors such as nitrogen vacancies, oxygen impurities, dislocations, dead layers, and nonuniform domains. Current research predominantly focuses on the macroscopic electrical performance of ferroelectric films, evaluating factors such as chemical composition, temperature characteristics, film size, deposition conditions, and cycle life. However, a deeper understanding of how defects influence the structure and ferroelectricity is lacking. To bridge this gap, future studies should employ theoretical calculations and in situ characterization techniques, such as high-precision in situ XRD and in situ STEM. Future research directions could prioritize reducing the coercive field in ultra-thin films and improving cycling performance to accelerate commercialization. The robust aluminum–nitrogen bonds and high nitrogen vacancy formation energy in the wurtzite crystal structure make AlN-based ferroelectrics well suited for applications in extreme environments, such as high-pressure and high-temperature conditions. Furthermore, the potential to transform non-ferroelectric materials into ferroelectric materials through

element doping, which flattens the energy landscape, provides a promising pathway for the discovery and design of new ferroelectric materials.

Author Contributions: L.W.: Conceptualization, Investigation, Methodology, Writing—Original Draft, Writing—Review and Editing. J.C.: Writing—Review and Editing. K.Q.: Conceptualization, Writing—Review and Editing, Supervision. Q.Z.: Conceptualization. B.T.: Supervision. Z.Y.: Methodology, Project Administration, Resources, Supervision. All authors have read and agreed to the published version of the manuscript.

Funding: We acknowledge financial support from the Shanghai Committee of Science and Technology (Grant No. 24JD1401200).

Data Availability Statement: No new data were created or analyzed in this study.

Conflicts of Interest: The authors declare no conflicts of interest.

References

1. Yang, H.; Sun, J.; Wang, H.; Li, H.; Yang, B. A review of oriented wurtzite-structure aluminum nitride films. *J. Alloys Compd.* **2024**, *989*, 174330. [CrossRef]
2. Liu, X.; Bruch, A.W.; Tang, H.X. Aluminum nitride photonic integrated circuits: From piezo-optomechanics to nonlinear optics. *Adv. Opt. Photonics* **2023**, *15*, 236–317. [CrossRef]
3. Iqbal, A.; Mohd-Yasin, F. Reactive sputtering of aluminum nitride (002) thin films for piezoelectric applications: A review. *Sensors* **2018**, *18*, 1797. [CrossRef]
4. Lin, B.-T.; Lee, W.-H.; Shieh, J.; Chen, M.-J. Ferroelectric AlN ultrathin films prepared by atomic layer epitaxy. In Proceedings of the Behavior and Mechanics of Multifunctional Materials XIII, Denver, CO, USA, 4–6 March 2019; pp. 287–293.
5. Hasegawa, K.; Shimizu, T.; Ohsawa, T.; Sakaguchi, I.; Ohashi, N. Full polarization reversal at room temperature in unsubstituted AlN. *Appl. Phys. Lett.* **2023**, *123*, 192903. [CrossRef]
6. Tasnádi, F.; Alling, B.; Höglund, C.; Wingqvist, G.; Birch, J.; Hultman, L.; Abrikosov, I.A. Origin of the anomalous piezoelectric response in wurtzite $Sc_xAl_{1-x}N$ alloys. *Phys. Rev. Lett.* **2010**, *104*, 137601. [CrossRef]
7. Fichtner, S.; Wolff, N.; Lofink, F.; Kienle, L.; Wagner, B. AlScN: A III-V semiconductor based ferroelectric. *J. Appl. Phys.* **2019**, *125*, 114103. [CrossRef]
8. Hayden, J.; Hossain, M.D.; Xiong, Y.; Ferri, K.; Zhu, W.; Imperatore, M.V.; Giebink, N.; Trolier-McKinstry, S.; Dabo, I.; Maria, J.-P. Ferroelectricity in boron-substituted aluminum nitride thin films. *Phys. Rev. Mater.* **2021**, *5*, 044412. [CrossRef]
9. Yasuoka, S.; Shimizu, T.; Tateyama, A.; Uehara, M.; Yamada, H.; Akiyama, M.; Hiranaga, Y.; Cho, Y.; Funakubo, H. Effects of deposition conditions on the ferroelectric properties of $(Al_{1-x}Sc_x)$ N thin films. *J. Appl. Phys.* **2020**, *128*, 114103. [CrossRef]
10. Zhu, W.; Hayden, J.; He, F.; Yang, J.-I.; Tipsawat, P.; Hossain, M.D.; Maria, J.-P.; Trolier-McKinstry, S. Strongly temperature dependent ferroelectric switching in AlN, Al1-xScxN, and Al1-xBxN thin films. *Appl. Phys. Lett.* **2021**, *119*, 062901. [CrossRef]
11. Wang, P.; Wang, D.; Mondal, S.; Mi, Z. Ferroelectric N-polar ScAlN/GaN heterostructures grown by molecular beam epitaxy. *Appl. Phys. Lett.* **2022**, *121*, 023501. [CrossRef]
12. Wolff, N.; Schönweger, G.; Streicher, I.; Islam, M.R.; Braun, N.; Straňák, P.; Kirste, L.; Prescher, M.; Lotnyk, A.; Kohlstedt, H. Demonstration and STEM Analysis of Ferroelectric Switching in MOCVD-Grown Single Crystalline $Al_{0.85}Sc_{0.15}N$. *Adv. Phys. Res.* **2024**, *3*, 2300113. [CrossRef]
13. Wang, D.; Mondal, S.; Liu, J.; Hu, M.; Wang, P.; Yang, S.; Wang, D.; Xiao, Y.; Wu, Y.; Ma, T. Ferroelectric YAlN grown by molecular beam epitaxy. *Appl. Phys. Lett.* **2023**, *123*, 033504. [CrossRef]
14. Yang, S.; Wang, D.; Tanim, M.M.H.; Wang, D.; Mi, Z. Molecular beam epitaxy and characterization of ferroelectric quaternary alloy $Sc_{0.2}Al_{0.45}Ga_{0.35}N$. *Appl. Phys. Lett.* **2024**, *124*, 193501. [CrossRef]
15. Fichtner, S.; Wolff, N.; Krishnamurthy, G.; Petraru, A.; Bohse, S.; Lofink, F.; Chemnitz, S.; Kohlstedt, H.; Kienle, L.; Wagner, B. Identifying and overcoming the interface originating c-axis instability in highly Sc enhanced AlN for piezoelectric micro-electromechanical systems. *J. Appl. Phys.* **2017**, *122*, 035301. [CrossRef]
16. Wang, D.; Wang, P.; Mondal, S.; Xiao, Y.; Hu, M.; Mi, Z. Impact of dislocation density on the ferroelectric properties of ScAlN grown by molecular beam epitaxy. *Appl. Phys. Lett.* **2022**, *121*, 042108. [CrossRef]
17. Guido, R.; Lomenzo, P.D.; Islam, M.R.; Wolff, N.; Gremmel, M.; Schönweger, G.; Kohlstedt, H.; Kienle, L.; Mikolajick, T.; Fichtner, S. Thermal stability of the ferroelectric properties in 100 nm-thick $Al_{0.72}Sc_{0.28}N$. *ACS Appl. Mater. Interfaces* **2023**, *15*, 7030–7043. [CrossRef] [PubMed]
18. Mikolajick, T.; Slesazeck, S.; Mulaosmanovic, H.; Park, M.; Fichtner, S.; Lomenzo, P.; Hoffmann, M.; Schroeder, U. Next generation ferroelectric materials for semiconductor process integration and their applications. *J. Appl. Phys.* **2021**, *129*, 100901. [CrossRef]

19. Casamento, J.; Baksa, S.M.; Behrendt, D.; Calderon, S.; Goodling, D.; Hayden, J.; He, F.; Jacques, L.; Lee, S.H.; Smith, W. Perspectives and progress on wurtzite ferroelectrics: Synthesis, characterization, theory, and device applications. *Appl. Phys. Lett.* **2024**, *124*, 080501. [CrossRef]
20. Liu, X.; Wang, D.; Kim, K.-H.; Katti, K.; Zheng, J.; Musavigharavi, P.; Miao, J.; Stach, E.A.; Olsson, R.H., III; Jariwala, D. Post-CMOS compatible aluminum scandium nitride/2D channel ferroelectric field-effect-transistor memory. *Nano Lett.* **2021**, *21*, 3753–3761. [CrossRef]
21. Liu, X.; Zheng, J.; Wang, D.; Musavigharavi, P.; Stach, E.A.; Olsson, R.; Jariwala, D. Aluminum scandium nitride-based metal–ferroelectric–metal diode memory devices with high on/off ratios. *Appl. Phys. Lett.* **2021**, *118*, 202901. [CrossRef]
22. Green, A.J.; Gillespie, J.K.; Fitch, R.C.; Walker, D.E.; Lindquist, M.; Crespo, A.; Brooks, D.; Beam, E.; Xie, A.; Kumar, V. ScAlN/GaN high-electron-mobility transistors with 2.4-A/mm current density and 0.67-S/mm transconductance. *IEEE Electron Device Lett.* **2019**, *40*, 1056–1059. [CrossRef]
23. Tian, B.; Wang, J.; Fusil, S.; Liu, Y.; Zhao, X.; Sun, S.; Shen, H.; Lin, T.; Sun, J.; Duan, C. Tunnel electroresistance through organic ferroelectrics. *Nat. Commun.* **2016**, *7*, 11502. [CrossRef] [PubMed]
24. Zhang, Y.; Zhu, Q.; Tian, B.; Duan, C. New-Generation Ferroelectric AlScN Materials. *Nano-Micro Lett.* **2024**, *16*, 227. [CrossRef] [PubMed]
25. Zheng, J.X.; Fiagbenu, M.M.A.; Esteves, G.; Musavigharavi, P.; Gunda, A.; Jariwala, D.; Stach, E.A.; Olsson, R.H. Ferroelectric behavior of sputter deposited $Al_{0.72}Sc_{0.28}N$ approaching 5 nm thickness. *Appl. Phys. Lett.* **2023**, *122*, 222901. [CrossRef]
26. Wang, P.; Wang, D.; Mondal, S.; Hu, M.; Liu, J.; Mi, Z. Dawn of nitride ferroelectric semiconductors: From materials to devices. *Semicond. Sci. Technol.* **2023**, *38*, 043002. [CrossRef]
27. Ryoo, S.K.; Kim, K.D.; Park, H.W.; Lee, Y.B.; Lee, S.H.; Lee, I.S.; Byun, S.; Shim, D.; Lee, J.H.; Kim, H. Investigation of optimum deposition conditions of radio frequency reactive magnetron sputtering of $Al_{0.7}Sc_{0.3}N$ film with thickness down to 20 nm. *Adv. Electron. Mater.* **2022**, *8*, 2200726. [CrossRef]
28. Wall, J.M.; Yan, F. Sputtering process of $Sc_xAl_{1-x}N$ thin films for ferroelectric applications. *Coatings* **2022**, *13*, 54. [CrossRef]
29. Schönweger, G.; Petraru, A.; Islam, M.R.; Wolff, N.; Haas, B.; Hammud, A.; Koch, C.; Kienle, L.; Kohlstedt, H.; Fichtner, S. From fully strained to relaxed: Epitaxial ferroelectric $Al_{1-x}Sc_xN$ for III-N technology. *Adv. Funct. Mater.* **2022**, *32*, 2109632. [CrossRef]
30. Casamento, J.; Xing, H.G.; Jena, D. Oxygen incorporation in the molecular beam epitaxy growth of $Sc_xGa_{1-x}N$ and $Sc_xAl_{1-x}N$. *Phys. Status Solidi B* **2020**, *257*, 1900612. [CrossRef]
31. Casamento, J.; Chang, C.S.; Shao, Y.-T.; Wright, J.; Muller, D.A.; Xing, H.G.; Jena, D. Structural and piezoelectric properties of ultra-thin $Sc_xAl_{1-x}N$ films grown on GaN by molecular beam epitaxy. *Appl. Phys. Lett.* **2020**, *117*, 112101. [CrossRef]
32. Leone, S.; Ligl, J.; Manz, C.; Kirste, L.; Fuchs, T.; Menner, H.; Prescher, M.; Wiegert, J.; Žukauskaitė, A.; Quay, R. Metal-organic chemical vapor deposition of aluminum scandium nitride. *Phys. Status Solidi RRL* **2020**, *14*, 1900535. [CrossRef]
33. Manz, C.; Leone, S.; Kirste, L.; Ligl, J.; Frei, K.; Fuchs, T.; Prescher, M.; Waltereit, P.; Verheijen, M.A.; Graff, A. Improved AlScN/GaN heterostructures grown by metal-organic chemical vapor deposition. *Semicond. Sci. Technol.* **2021**, *36*, 034003. [CrossRef]
34. Ligl, J.; Leone, S.; Manz, C.; Kirste, L.; Doering, P.; Fuchs, T.; Prescher, M.; Ambacher, O. Metalorganic chemical vapor phase deposition of AlScN/GaN heterostructures. *J. Appl. Phys.* **2020**, *127*, 19. [CrossRef]
35. Leone, S.; Streicher, I.; Prescher, M.; Straňák, P.; Kirste, L. Metal-Organic Chemical Vapor Deposition of Aluminum Yttrium Nitride. *Phys. Status Solidi (RRL)–Rapid Res. Lett.* **2023**, *17*, 2300091. [CrossRef]
36. Yang, W.; Wang, W.; Lin, Y.; Liu, Z.; Zhou, S.; Qian, H.; Gao, F.; Zhang, S.; Li, G. Deposition of nonpolar m-plane InGaN/GaN multiple quantum wells on $LiGaO_2$ (100) substrates. *J. Mater. Chem. C* **2014**, *2*, 801–805. [CrossRef]
37. Li, G.; Ohta, J.; Kobayashi, A.; Fujioka, H. Room-temperature epitaxial growth of AlN on atomically flat $MgAl_2O_4$ substrates. *Appl. Phys. Lett.* **2006**, *89*, 182104. [CrossRef]
38. Li, G.; Wang, W.; Yang, W.; Wang, H. Epitaxial growth of group III-nitride films by pulsed laser deposition and their use in the development of LED devices. *Surf. Sci. Rep.* **2015**, *70*, 380–423. [CrossRef]
39. Yang, H.; Wang, W.; Liu, Z.; Li, G. Homogeneous epitaxial growth of AlN single-crystalline films on 2 inch-diameter Si (111) substrates by pulsed laser deposition. *CrystEngComm* **2013**, *15*, 7171–7176. [CrossRef]
40. Okamoto, K.; Inoue, S.; Nakano, T.; Kim, T.-W.; Oshima, M.; Fujioka, H. Epitaxial growth of AlN on single crystal Mo substrates. *Thin Solid Film.* **2008**, *516*, 4809–4812. [CrossRef]
41. Wang, W.; Yang, W.; Liu, Z.; Lin, Y.; Zhou, S.; Qian, H.; Gao, F.; Yang, H.; Li, G. Epitaxial growth of homogeneous single-crystalline AlN films on single-crystalline Cu (1 1 1) substrates. *Appl. Surf. Sci.* **2014**, *294*, 1–8. [CrossRef]
42. Ohta, J.; Fujioka, H.; Takahashi, H.; Oshima, M. Characterization of hetero-interfaces between group III nitrides formed by PLD and various substrates. *Appl. Surf. Sci.* **2002**, *190*, 352–355. [CrossRef]
43. Chen, L.; Wang, Q.; Liu, C.; Li, M.; Song, W.; Wang, W.; Loke, D.K.; Zhu, Y. Leakage Mechanism and Cycling Behavior of Ferroelectric $Al_{0.7}Sc_{0.3}N$. *Materials* **2024**, *17*, 397. [CrossRef] [PubMed]

44. Kizir, S.; Haider, A.; Biyikli, N. Substrate impact on the low-temperature growth of GaN thin films by plasma-assisted atomic layer deposition. *J. Vac. Sci. Technol. A* **2016**, *34*, 041511. [CrossRef]
45. Strnad, N.A.; Sarney, W.L.; Rayner, G.B.; Benoit, R.R.; Fox, G.R.; Rudy, R.Q.; Larrabee, T.J.; Shallenberger, J.; Pulskamp, J.S. Plasma enhanced atomic layer deposition of textured aluminum nitride on platinized substrates for MEMS. *J. Vac. Sci. Technol. A* **2022**, *40*, 042403. [CrossRef]
46. Tian, L.; Ponton, S.; Benz, M.; Crisci, A.; Reboud, R.; Giusti, G.; Volpi, F.; Rapenne, L.; Vallée, C.; Pons, M. Aluminum nitride thin films deposited by hydrogen plasma enhanced and thermal atomic layer deposition. *Surf. Coat. Technol.* **2018**, *347*, 181–190. [CrossRef]
47. Kao, W.-C.; Lee, W.-H.; Yi, S.-H.; Shen, T.-H.; Lin, H.-C.; Chen, M.-J. AlN epitaxy on SiC by low-temperature atomic layer deposition via layer-by-layer, in situ atomic layer annealing. *RSC Adv.* **2019**, *9*, 12226–12231. [CrossRef]
48. Kot, M.; Henkel, K.; Naumann, F.; Gargouri, H.; Lupina, L.; Wilker, V.; Kus, P.; Garain, S.; Rouissi, Z.; Schmeißer, D. Comparison of plasma-enhanced atomic layer deposition AlN films prepared with different plasma sources. *J. Vac. Sci. Technol. A* **2019**, *37*, 020913. [CrossRef]
49. Ilhom, S.; Shukla, D.; Mohammad, A.; Grasso, J.; Willis, B.; Biyikli, N. Understanding the role of rf-power on AlN film properties in hollow-cathode plasma-assisted atomic layer deposition. *J. Vac. Sci. Technol. A* **2020**, *38*, 022405. [CrossRef]
50. Musavigharavi, P.; Meng, A.C.; Wang, D.; Zheng, J.; Foucher, A.C.; Olsson III, R.H.; Stach, E.A. Nanoscale structural and chemical properties of ferroelectric aluminum scandium nitride thin films. *J. Phys. Chem. C* **2021**, *125*, 14394–14400. [CrossRef]
51. Islam, M.R.; Wolff, N.; Yassine, M.; Schönweger, G.; Christian, B.; Kohlstedt, H.; Ambacher, O.; Lofink, F.; Kienle, L.; Fichtner, S. On the exceptional temperature stability of ferroelectric $Al_{1-x}Sc_xN$ thin films. *Appl. Phys. Lett.* **2021**, *118*, 232905. [CrossRef]
52. Wolff, N.; Fichtner, S.; Haas, B.; Islam, M.R.; Niekiel, F.; Kessel, M.; Ambacher, O.; Koch, C.; Wagner, B.; Lofink, F. Atomic scale confirmation of ferroelectric polarization inversion in wurtzite-type AlScN. *J. Appl. Phys.* **2021**, *129*, 034103. [CrossRef]
53. Wang, D.; Musavigharavi, P.; Zheng, J.; Esteves, G.; Liu, X.; Fiagbenu, M.M.A.; Stach, E.A.; Jariwala, D.; Olsson III, R.H. Sub-microsecond polarization switching in (Al, Sc) N ferroelectric capacitors grown on complementary metal–oxide–semiconductor-compatible aluminum electrodes. *Phys. Status Solidi RRL* **2021**, *15*, 2000575. [CrossRef]
54. Yasuoka, S.; Mizutani, R.; Ota, R.; Shiraishi, T.; Shimizu, T.; Uehara, M.; Yamada, H.; Akiyama, M.; Funakubo, H. Tunable ferroelectric properties in wurtzite $(Al_{0.8}Sc_{0.2})$ N via crystal anisotropy. *ACS Appl. Electron. Mater.* **2022**, *4*, 5165–5170. [CrossRef]
55. Casamento, J.; Lee, H.; Maeda, T.; Gund, V.; Nomoto, K.; van Deurzen, L.; Turner, W.; Fay, P.; Mu, S.; Van de Walle, C.G. Epitaxial $Sc_xAl_{1-x}N$ on GaN exhibits attractive high-K dielectric properties. *Appl. Phys. Lett.* **2022**, *120*, 152901. [CrossRef]
56. Yuan, C.; Park, M.; Zheng, Y.; Shi, J.; Dargis, R.; Graham, S.; Ansari, A. Phonon heat conduction in Al1-xScxN thin films. *Mater. Today Phys.* **2021**, *21*, 100498. [CrossRef]
57. Park, M.; Hao, Z.; Dargis, R.; Clark, A.; Ansari, A. Epitaxial aluminum scandium nitride super high frequency acoustic resonators. *J. Microelectromech. Syst.* **2020**, *29*, 490–498. [CrossRef]
58. Hardy, M.T.; Jin, E.N.; Nepal, N.; Katzer, D.S.; Downey, B.P.; Gokhale, V.J.; Storm, D.F.; Meyer, D.J. Control of phase purity in high scandium fraction heteroepitaxial ScAlN grown by molecular beam epitaxy. *Appl. Phys. Express* **2020**, *13*, 065509. [CrossRef]
59. Krause, S.; Streicher, I.; Waltereit, P.; Kirste, L.; Brückner, P.; Leone, S. AlScN/GaN HEMTs grown by metal-organic chemical vapor deposition with 8.4 W/mm output power and 48% power-added efficiency at 30 GHz. *IEEE Electron Device Lett.* **2022**, *44*, 17–20. [CrossRef]
60. Chen, L.; Liu, C.; Li, M.; Song, W.; Wang, W.; Chen, Z.; Samanta, S.; Lee, H.K.; Zhu, Y. Bipolar and unipolar cycling behavior in ferroelectric scandium-doped aluminum nitride. In Proceedings of the 2022 IEEE International Symposium on Applications of Ferroelectrics (ISAF), Tours, France, 27 June–1 July 2022; pp. 1–3.
61. Liu, C.; Wang, Q.; Yang, W.; Cao, T.; Chen, L.; Li, M.; Liu, F.; Loke, D.; Kang, J.; Zhu, Y. Multiscale Modeling of $Al_{0.7}Sc_{0.3}$ N-based FeRAM: The steep switching, leakage and selector-free array. In Proceedings of the 2021 IEEE International Electron Devices Meeting (IEDM), San Francisco, CA, USA, 11–16 December 2021; pp. 8.1. 1–8.1. 4.
62. Liu, X.; Ting, J.; He, Y.; Fiagbenu, M.M.A.; Zheng, J.; Wang, D.; Frost, J.; Musavigharavi, P.; Esteves, G.; Kisslinger, K. Reconfigurable compute-in-memory on field-programmable ferroelectric diodes. *Nano Lett.* **2022**, *22*, 7690–7698. [CrossRef] [PubMed]
63. Wang, D.; Zheng, J.; Musavigharavi, P.; Zhu, W.; Foucher, A.C.; Trolier-McKinstry, S.E.; Stach, E.A.; Olsson, R.H. Ferroelectric switching in sub-20 nm aluminum scandium nitride thin films. *IEEE Electron Device Lett.* **2020**, *41*, 1774–1777. [CrossRef]
64. Wang, P.; Wang, D.; Vu, N.M.; Chiang, T.; Heron, J.T.; Mi, Z. Fully epitaxial ferroelectric ScAlN grown by molecular beam epitaxy. *Appl. Phys. Lett.* **2021**, *118*, 223504. [CrossRef]
65. Yasuoka, S.; Shimizu, T.; Tateyama, A.; Uehara, M.; Yamada, H.; Akiyama, M.; Funakubo, H. Impact of Deposition Temperature on Crystal Structure and Ferroelectric Properties of $(Al_{1-x}Sc_x)$ N Films Prepared by Sputtering Method. *Phys. Status Solidi A* **2021**, *218*, 2100302. [CrossRef]

66. Zheng, Y.; Wang, J.; Park, M.; Wang, P.; Wang, D.; Mi, Z.; Ansari, A. High-order Sezawa mode Alscn/Gan/sapphire surface acoustic wave resonators. In Proceedings of the 2022 IEEE 35th International Conference on Micro Electro Mechanical Systems Conference (MEMS), Tokyo, Japan, 9–13 January 2022; pp. 1046–1049.
67. Zhu, W.; He, F.; Hayden, J.; Fan, Z.; Yang, J.I.; Maria, J.P.; Trolier-McKinstry, S. Wake-up in $Al_{1-x}B_xN$ ferroelectric films. *Adv. Electron. Mater.* **2022**, *8*, 2100931. [CrossRef]
68. Zhu, W.; He, F.; Hayden, J.; Yang, J.I.; Tipsawat, P.; Maria, J.-P.; Trolier-McKinstry, S. Exceptional high temperature retention in $Al_{0.93}B_{0.07}N$ films. *Appl. Phys. Lett.* **2023**, *122*, 242902. [CrossRef]
69. Moriwake, H.; Konishi, A.; Ogawa, T.; Fujimura, K.; Fisher, C.A.; Kuwabara, A.; Shimizu, T.; Yasui, S.; Itoh, M. Ferroelectricity in wurtzite structure simple chalcogenide. *Appl. Phys. Lett.* **2014**, *104*, 242909. [CrossRef]
70. Konishi, A.; Ogawa, T.; Fisher, C.A.; Kuwabara, A.; Shimizu, T.; Yasui, S.; Itoh, M.; Moriwake, H. Mechanism of polarization switching in wurtzite-structured zinc oxide thin films. *Appl. Phys. Lett.* **2016**, *109*, 150–153. [CrossRef]
71. Satoh, S.; Ohtaka, K.; Shimatsu, T.; Tanaka, S. Crystal structure deformation and phase transition of AlScN thin films in whole Sc concentration range. *J. Appl. Phys.* **2022**, *132*, 025103. [CrossRef]
72. Zhang, X.; Xu, W.; Meng, W.; Meng, A.C. Single crystal ferroelectric AlScN nanowires. *CrystEngComm* **2024**, *26*, 180–191. [CrossRef]
73. Schönweger, G.; Wolff, N.; Islam, M.R.; Gremmel, M.; Petraru, A.; Kienle, L.; Kohlstedt, H.; Fichtner, S. In-grain ferroelectric switching in sub-5 nm thin $Al_{0.74}Sc_{0.26}N$ films at 1 V. *Adv. Sci.* **2023**, *10*, 2302296. [CrossRef]
74. Visconti, P.; Huang, D.; Reshchikov, M.; Yun, F.; Cingolani, R.; Smith, D.; Jasinski, J.; Swider, W.; Liliental-Weber, Z.; Morkoc, H. Investigation of defects and surface polarity in GaN using hot wet etching together with microscopy and diffraction techniques. *Mater. Sci. Eng. B* **2002**, *93*, 229–233. [CrossRef]
75. Deng, R.; Evans, S.R.; Gall, D. Bandgap in $Al_{1-x}Sc_xn$. *Appl. Phys. Lett.* **2013**, *102*, 112103. [CrossRef]
76. Akiyama, M.; Kamohara, T.; Kano, K.; Teshigahara, A.; Takeuchi, Y.; Kawahara, N. Enhancement of piezoelectric response in scandium aluminum nitride alloy thin films prepared by dual reactive cosputtering. *Adv. Mater.* **2009**, *21*, 593–596. [CrossRef] [PubMed]
77. Calderon, S.; Hayden, J.; Baksa, S.M.; Tzou, W.; Trolier-McKinstry, S.; Dabo, I.; Maria, J.-P.; Dickey, E.C. Atomic-scale polarization switching in wurtzite ferroelectrics. *Science* **2023**, *380*, 1034–1038. [CrossRef]
78. Mayrhofer, P.; Riedl, H.; Euchner, H.; Stöger-Pollach, M.; Mayrhofer, P.H.; Bittner, A.; Schmid, U. Microstructure and piezoelectric response of $Y_xAl_{1-x}N$ thin films. *Acta Mater.* **2015**, *100*, 81–89. [CrossRef]
79. Winiarski, M.J.; Kowalska, D. Electronic structure of REN (RE = Sc, Y, La, and Lu) semiconductors by MBJLDA calculations. *Mater. Res. Express* **2019**, *6*, 095910. [CrossRef]
80. Ramirez-Montes, L.; Lopez-Perez, W.; Gonzalez-Garcia, A.; Gonzalez-Hernandez, R. Structural, optoelectronic, and thermodynamic properties of Y _x x Al _ 1-x 1-x N semiconducting alloys. *J. Mater. Sci.* **2016**, *51*, 2817–2829. [CrossRef]
81. Manna, S.; Brennecka, G.L.; Stevanović, V.; Ciobanu, C.V. Tuning the piezoelectric and mechanical properties of the AlN system via alloying with YN and BN. *J. Appl. Phys.* **2017**, *122*, 105101. [CrossRef]
82. Schlögl, M.; Schneider, M.; Schmid, U. Piezoelectricity in $Y_{0.09}Al_{0.91}N$ thin films. *Mater. Sci. Eng. B* **2022**, *276*, 115543. [CrossRef]
83. Yang, L.; Wang, X.; Wang, T.; Wang, J.; Zhang, W.; Quach, P.; Wang, P.; Liu, F.; Li, D.; Chen, L. Three subband occupation of the two-dimensional electron gas in ultrathin barrier AlN/GaN heterostructures. *Adv. Funct. Mater.* **2020**, *30*, 2004450. [CrossRef]
84. Wang, P.; Wang, D.; Bi, Y.; Wang, B.; Schwartz, J.; Hovden, R.; Mi, Z. Quaternary alloy ScAlGaN: A promising strategy to improve the quality of ScAlN. *Appl. Phys. Lett.* **2022**, *120*, 012104. [CrossRef]
85. Wang, D.; Wang, P.; Mondal, S.; Mohanty, S.; Ma, T.; Ahmadi, E.; Mi, Z. An epitaxial ferroelectric ScAlN/GaN heterostructure memory. *Adv. Electron. Mater.* **2022**, *8*, 2200005. [CrossRef]
86. Yazawa, K.; Zakutayev, A.; Brennecka, G.L. A Landau–Devonshire analysis of strain effects on ferroelectric $Al_{1-x}Sc_xN$. *Appl. Phys. Lett.* **2022**, *121*, 042902. [CrossRef]
87. Rajamani, A.; Sheldon, B.W.; Chason, E.; Bower, A.F. Intrinsic tensile stress and grain boundary formation during Volmer–Weber film growth. *Appl. Phys. Lett.* **2002**, *81*, 1204–1206. [CrossRef]
88. Panda, P.; Ramaseshan, R.; Ravi, N.; Mangamma, G.; Jose, F.; Dash, S.; Suzuki, K.; Suematsu, H. Reduction of residual stress in AlN thin films synthesized by magnetron sputtering technique. *Mater. Chem. Phys.* **2017**, *200*, 78–84. [CrossRef]
89. Islam, M.R.; Schönweger, G.; Wolff, N.; Petraru, A.; Kohlstedt, H.; Fichtner, S.; Kienle, L. A comparative study of $Pt/Al_{0.72}Sc_{0.28}N/Pt$-based thin-film metal-ferroelectric-metal capacitors on GaN and Si substrates. *ACS Appl. Mater. Interfaces* **2023**, *15*, 41606–41613. [CrossRef]
90. Chen, L.; Wang, Z.; Liu, C.; Li, M.; Song, W.; Wang, W.; Varghese, B.; Lee, H.K.; Lin, H.; Zhu, Y. Leakage mechanism of ferroelectric $Al_{0.7}Sc_{0.3}N$ ultra-thin film. In Proceedings of the 2023 IEEE International Symposium on Applications of Ferroelectrics (ISAF), Cleveland, OH, USA, 23–27 July 2023; pp. 1–3.
91. Liu, M.; Zang, H.; Jia, Y.; Jiang, K.; Ben, J.; Lv, S.; Li, D.; Sun, X.; Li, D. Effect and Regulation Mechanism of Post-deposition Annealing on the Ferroelectric Properties of AlScN Thin Films. *ACS Appl. Mater. Interfaces* **2024**, *16*, 16427–16435. [CrossRef]

92. Mohn, S.; Stolyarchuk, N.; Markurt, T.; Kirste, R.; Hoffmann, M.P.; Collazo, R.; Courville, A.; Di Felice, R.; Sitar, Z.; Vennéguès, P. Polarity control in group-III nitrides beyond pragmatism. *Phys. Rev. Appl.* **2016**, *5*, 054004. [CrossRef]
93. Zheng, J.X.; Wang, D.; Musavigharavi, P.; Fiagbenu, M.M.A.; Jariwala, D.; Stach, E.A.; Olsson, R.H. Electrical breakdown strength enhancement in aluminum scandium nitride through a compositionally modulated periodic multilayer structure. *J. Appl. Phys.* **2021**, *130*, 144101. [CrossRef]
94. Chen, L.; Liu, C.; Wang, Z.; Li, M.; Song, W.; Wang, W.; Zhu, Y. In-wafer stress-dependent leakage current in ferroelectric scandium-doped aluminum nitride. In Proceedings of the 2023 IEEE International Symposium on Applications of Ferroelectrics (ISAF), Cleveland, OH, USA, 23–27 July 2023; pp. 1–3.
95. Yang, W.; Chen, L.; Li, M.; Liu, F.; Liu, X.; Liu, C.; Kang, J. Stress effect on the leakage current distribution of ferroelectric $Al_{0.7}Sc_{0.3}N$ across the wafer. *Appl. Phys. Lett.* **2023**, *123*, 132903. [CrossRef]
96. Fichtner, S.; Reimer, T.; Chemnitz, S.; Lofink, F.; Wagner, B. Stress controlled pulsed direct current co-sputtered $Al_{1-x}Sc_xN$ as piezoelectric phase for micromechanical sensor applications. *APL Mater.* **2015**, *3*, 116102. [CrossRef]
97. Beaucejour, R.; Roebisch, V.; Kochhar, A.; Moe, C.G.; Hodge, M.D.; Olsson, R.H. Controlling residual stress and suppression of anomalous grains in aluminum scandium nitride films grown directly on silicon. *J. Microelectromech. Syst.* **2022**, *31*, 604–611. [CrossRef]
98. Yang, J.; Luo, Q.; Xue, X.; Jiang, H.; Wu, Q.; Han, Z.; Cao, Y.; Han, Y.; Dou, C.; Lv, H. A 9Mb HZO-based embedded FeRAM with 10 12-cycle endurance and 5/7ns read/write using ECC-assisted data refresh and offset-canceled sense amplifier. In Proceedings of the 2023 IEEE International Solid-State Circuits Conference (ISSCC), San Francisco, CA, USA, 19–23 February 2023; pp. 1–3.
99. Wang, R.; Yao, D.; Zhou, J.; Li, Y.; Jiang, Z.; Chen, D.; Ran, X.; Gao, Y.; Cheng, Z.; Wang, Y. Microscopic Insights into Fatigue Mechanism in Wurtzite Ferroelectric $Al_{0.65}Sc_{0.35}N$: Oxygen Infiltration Enabled Grain Amorphization Spanning Boundary to Bulk. *arXiv* **2024**. *preprint*.
100. Kim, K.D.; Lee, Y.B.; Lee, S.H.; Lee, I.S.; Ryoo, S.K.; Byun, S.; Lee, J.H.; Kim, H.; Park, H.W.; Hwang, C.S. Evolution of the ferroelectric properties of AlScN film by electrical cycling with an inhomogeneous field distribution. *Adv. Electron. Mater.* **2023**, *9*, 2201142. [CrossRef]
101. Kim, K.-H.; Oh, S.; Fiagbenu, M.M.A.; Zheng, J.; Musavigharavi, P.; Kumar, P.; Trainor, N.; Aljarb, A.; Wan, Y.; Kim, H.M. Scalable CMOS back-end-of-line-compatible AlScN/two-dimensional channel ferroelectric field-effect transistors. *Nat. Nanotechnol.* **2023**, *18*, 1044–1050. [CrossRef] [PubMed]
102. Wang, P.; Wang, D.; Mondal, S.; Hu, M.; Wu, Y.; Ma, T.; Mi, Z. Ferroelectric nitride heterostructures on CMOS compatible molybdenum for synaptic memristors. *ACS Appl. Mater. Interfaces* **2023**, *15*, 18022–18031. [CrossRef]
103. Wang, J.; Zheng, Y.; Ansari, A. Ferroelectric aluminum scandium nitride thin film bulk acoustic resonators with polarization-dependent operating states. *Phys. Status Solidi RRL* **2021**, *15*, 2100034. [CrossRef]
104. Do Kim, K.; Lee, Y.B.; Lee, S.H.; Lee, I.S.; Ryoo, S.K.; Byun, S.Y.; Lee, J.H.; Hwang, C.S. Impact of operation voltage and NH 3 annealing on the fatigue characteristics of ferroelectric AlScN thin films grown by sputtering. *Nanoscale* **2023**, *15*, 16390–16402. [CrossRef]
105. Chen, S.-M.; Hoshii, T.; Wakabayashi, H.; Tsutsui, K.; Chang, E.Y.; Kakushima, K. Reactive sputtering of ferroelectric AlScN films with H2 gas flow for endurance improvement. *Jpn. J. Appl. Phys.* **2024**, *63*, 03SP45. [CrossRef]
106. He, F.; Zhu, W.; Hayden, J.; Casamento, J.; Tran, Q.; Kang, K.; Song, Y.; Akkopru-Akgun, B.; Yang, J.I.; Tipsawat, P. Frequency dependence of wake-up and fatigue characteristics in ferroelectric $Al_{0.93}B_{0.07}N$ thin films. *Acta Mater.* **2024**, *266*, 119678. [CrossRef]
107. Sui, W.; Wang, H.; Lee, J.; Qamar, A.; Rais-Zadeh, M.; Feng, P.X.L. AlScN-on-SiC Thin Film Micromachined Resonant Transducers Operating in High-Temperature Environment up to 600 °C. *Adv. Funct. Mater.* **2022**, *32*, 2202204. [CrossRef]
108. Lin, C.-M.; Yen, T.-T.; Felmetsger, V.V.; Hopcroft, M.A.; Kuypers, J.H.; Pisano, A.P. Thermally compensated aluminum nitride Lamb wave resonators for high temperature applications. *Appl. Phys. Lett.* **2010**, *97*, 083501. [CrossRef]
109. Pozzi, M.; Hassan, M.; Harris, A.J.; Burdess, J.S.; Jiang, L.; Lee, K.K.; Cheung, R.; Phelps, G.J.; Wright, N.G.; Zorman, C.A. Mechanical properties of a 3C-SiC film between room temperature and 600 C. *J. Phys. D Appl. Phys.* **2007**, *40*, 3335. [CrossRef]
110. Rodriguez, J.A.; Remack, K.; Boku, K.; Udayakumar, K.; Aggarwal, S.; Summerfelt, S.R.; Celii, F.G.; Martin, S.; Hall, L.; Taylor, K. Reliability properties of low-voltage ferroelectric capacitors and memory arrays. *IEEE Trans. Device Mater. Reliab.* **2004**, *4*, 436–449. [CrossRef]
111. Pradhan, D.K.; Moore, D.C.; Kim, G.; He, Y.; Musavigharavi, P.; Kim, K.-H.; Sharma, N.; Han, Z.; Du, X.; Puli, V.S. Scalable and Stable Ferroelectric Non-Volatile Memory at> 500 °C. *arXiv* **2023**. *preprint*.
112. Österlund, E.; Ross, G.; Caro, M.A.; Paulasto-Kröckel, M.; Hollmann, A.; Klaus, M.; Meixner, M.; Genzel, C.; Koppinen, P.; Pensala, T. Stability and residual stresses of sputtered wurtzite AlScN thin films. *Phys. Rev. Mater.* **2021**, *5*, 035001. [CrossRef]
113. Wolff, N.; Islam, M.R.; Kirste, L.; Fichtner, S.; Lofink, F.; Žukauskaitė, A.; Kienle, L. $Al_{1-x}Sc_xN$ thin films at high temperatures: Sc-dependent instability and anomalous thermal expansion. *Micromachines* **2022**, *13*, 1282. [CrossRef] [PubMed]
114. Casamento, J.; Nguyen, T.-S.; Cho, Y.; Savant, C.; Vasen, T.; Afroz, S.; Hannan, D.; Xing, H.G.; Jena, D. Transport properties of polarization-induced 2D electron gases in epitaxial AlScN/GaN heterojunctions. *Appl. Phys. Lett.* **2022**, *121*, 192101. [CrossRef]

115. Wang, D.; Mondal, S.; Kezer, P.; Hu, M.; Liu, J.; Wu, Y.; Zhou, P.; Ma, T.; Wang, P.; Wang, D. Band alignment and charge carrier transport properties of YAlN/III-nitride heterostructures. *Appl. Surf. Sci.* **2023**, *637*, 157893. [CrossRef]
116. Yoshioka, V.; Jin, J.; Zhou, H.; Tang, Z.; Olsson III, R.H.; Zhen, B. CMOS-compatible, AlScN-based integrated electro-optic phase shifter. *Nanophotonics* **2024**, *13*, 3327–3335. [CrossRef]
117. Huang, C.; Shi, H.; Yu, L.; Wang, K.; Cheng, M.; Huang, Q.; Jiao, W.; Sun, J. Acousto-optic modulation in silicon waveguides based on piezoelectric aluminum scandium nitride film. *Adv. Opt. Mater.* **2022**, *10*, 2102334. [CrossRef]
118. Friedman, B.; Barth, S.; Schreiber, T.; Bartzsch, H.; Bain, J.; Piazza, G. Measured optical losses of Sc doped AlN waveguides. *Opt. Express* **2024**, *32*, 5252–5260. [CrossRef] [PubMed]
119. Mondal, S.; Wang, D.; Wang, P.; Wu, Y.; Hu, M.; Xiao, Y.; Mohanty, S.; Ma, T.; Ahmadi, E.; Mi, Z. Reconfigurable self-powered deep UV photodetectors based on ultrawide bandgap ferroelectric ScAlN. *APL Mater.* **2022**, *10*, 121101. [CrossRef]
120. Huang, C.; Shi, H.; Yu, L.; Huang, Q.; Zhang, T.; Xue, H.; Sun, J. Intramodal and Intermodal Modulations in Exposed Silicon Waveguides with Surface Acoustic Waves Excited by Aluminum Scandium Nitride Films. *ACS Photonics* **2024**, *11*, 1950–1959. [CrossRef]
121. Bian, K.; Li, Z.; Liu, Y.; Xu, S.; Zhao, X.; Qiu, Y.; Dong, Y.; Zhong, Q.; Wu, T.; Zheng, S. Demonstration of acousto-optical modulation based on a thin-film AlScN photonic platform. *Photonics Res.* **2024**, *12*, 1138–1149. [CrossRef]

Disclaimer/Publisher's Note: The statements, opinions and data contained in all publications are solely those of the individual author(s) and contributor(s) and not of MDPI and/or the editor(s). MDPI and/or the editor(s) disclaim responsibility for any injury to people or property resulting from any ideas, methods, instructions or products referred to in the content.